The Astrophysical Journal, 908:92 (19pp), 2021 February 10 https://doi.org/10.3847/1538-4357/abd034

Rotating Filament in Orion B: Do Cores Inherit Their Angular Momentum from Their Parent Filament?

Cheng-Han Hsieh (承翰)[1], Héctor G. Arce[1], Diego Mardones[2], Shuo Kong[1,3], and Adele Plunkett[4]
[1] Department of Astronomy, Yale University, New Haven, CT 06511, USA; cheng-han.hsieh@yale.edu
[2] Departamento de Astronomia, Universidad de Chile, Casilla 36-D, Santiago, Chile
[3] Steward Observatory, University of Arizona, Tucson, AZ 85719, USA
[4] National Radio Astronomy Observatory, 520 Edgemont Road, Charlottesville, VA 22903, USA
Received 2020 March 8; revised 2020 November 30; accepted 2020 December 1; published 2021 February 16

Abstract

Angular momentum is one of the most important physical quantities that governs star formation. The initial angular momentum of a core may be responsible for its fragmentation, and can have an influence on the size of the protoplanetary disk. To understand how cores obtain their initial angular momentum, it is important to study the angular momentum of filaments where they form. While theoretical studies on filament rotation have been explored, there exist very few observational measurements of the specific angular momentum in star-forming filaments. We present high-resolution N_2D^+ ALMA observations of the LBS 23 (HH24-HH26) region in Orion B, which provide one of the most reliable measurements of the specific angular momentum in a star-forming filament. We find the total specific angular momentum (4×10^{20} cm^2 s^{-1}), the dependence of the specific angular momentum with radius ($j(r) \propto r^{1.83}$), and the ratio of rotational energy to gravitational energy ($\beta_{\rm rot} \sim 0.04$) comparable to those observed in rotating cores with sizes similar to our filament width (~0.04 pc) in other star-forming regions. Our filament angular momentum profile is consistent with rotation acquired from ambient turbulence and with simulations that show cores and their host filaments develop simultaneously due to multi-scale growth of nonlinear perturbation generated by turbulence.

Unified Astronomy Thesaurus concepts: Star formation (1569); Observational astronomy (1145); Interstellar filaments (842); Stellar cores (1592); Molecular clouds (1072); Giant molecular clouds (653); Young stellar objects (1834); Protostars (1302); Herbig-Haro objects (722); Star forming regions (1565); Interstellar medium (847); Radio interferometry (1346)

1. Introduction

One of the main challenges in star formation is trying to solve the so-called "angular momentum problem," which arises from the fact that the observed angular momentum of individual stars is much smaller than that of molecular cloud cores from which they presumably formed (Larson 2003; Jappsen & Klessen 2004). At large molecular cloud scales (~10 pc), where the density is low and the ionization fraction is high (~10^{-6}) (Tielens 2005), magnetic braking effects may be effective in removing most of the angular momentum (Basu & Mouschovias 1994; Crutcher 1999). At smaller scales, studies conducted about two to three decades ago found that the specific angular momentum[5] of cores is comparable to that of wide separation binaries (~1000 au) (Goodman et al. 1993; Barranco & Goodman 1998; Jijina et al. 1999; Caselli et al. 2002). Other observations also found that, at scales smaller than 0.03 pc, the angular momentum is conserved (Ohashi et al. 1997; Myers et al. 2000; Belloche et al. 2002; Belloche 2013; Li et al. 2014), which is consistent with the theoretical prediction of weaker magnetic braking effects at smaller scales (Basu 1997). The question of how cores obtain their initial angular momentum remains an important and heated topic today in star formation, as it sets the angular momentum budget for the formation of multiple systems and protoplanetary disks.

Recent Herschel studies have shown that most stars form in filaments with a supposed universal width of 0.1 pc (André et al. 2010; Arzoumanian et al. 2011, 2019; Koch & Rosolowsky 2015; Tafalla & Hacar 2015). If most cores are formed in filaments (André et al. 2014), one would expect then that filament rotation and fragmentation could play an important role in explaining the origin of core angular momentum.

One possible explanation for the origin of core angular momentum is turbulence. A recent theoretical study by Misugi et al. (2019) found the observed dependence of specific angular momentum with mass can be explained by one-dimensional Kolmogorov (isotropic) turbulence perturbations in filaments. While their results are consistent with observations, this model is likely far from complete, as it does not incorporate magnetic fields, which are thought to be important at filament scales (Palmeirim et al. 2013) and result in anisotropic turbulence. Moreover, Misugi et al. (2019) does not consider how the global filament rotation affects the initial angular momentum of cores.

While a number of numerical studies show that turbulence may provide the initial angular momentum in cores (e.g., Burkert & Bodenheimer 2000; Chen & Ostriker 2018; Misugi et al. 2019), some simulations underestimate the core angular momentum by a factor of 10 compared to values derived from observations (e.g., Offner et al. 2008; Dib et al. 2010). Dib et al. (2010) compared the intrinsic angular momentum ($j_{\rm 3D}$) in their simulated cores to synthetic specific angular momentum derived from two-dimensional velocity maps ($j_{\rm 2D}$) and found $j_{\rm 3D}/j_{\rm 2D} \sim 0.1$, which suggest observations overestimate the true angular momenta by an order of magnitude. However, Zhang et al. (2018) suggest this order-of-magnitude difference comes not from observational error but is instead possibly due

[5] Specific angular momentum is defined as angular momentum per unit mass.

to numerical effects. More recently, Kuznetsova et al. (2019) conducted a conservative order-of-magnitude calculation and showed the resulting angular momentum to be an order of magnitude below the minimum angular momentum observed in cores, possibly indicating that the model of turbulent origin for the angular momentum in cores is inconsistent with observations. However, the theoretical turbulent models of Misugi et al. (2019) tend to reproduce observations well with reasonable parameters. A turbulence-induced origin for the angular momentum in cores cannot yet be ruled out.

In contrast with most previous studies, Kuznetsova et al. (2019) propose that the initial angular momentum of cores is generated locally and comes from the gravitational interactions of overdensities (dense cores), and it is not inherited from the large-scale initial cloud rotation. Thus, there is still no consensus on the origin of angular momentum in cores.

Filaments, which lie at intermediate scales between molecular cloud scales (∼10 pc) and the small core/envelope scales (∼0.01 pc) might be the key for understanding the origin of a core's initial angular momentum. Observations of the L1251 infrared dark cloud found that this ∼3.3 pc × 0.3 pc filament is rotating along its minor axis with an angular frequency (ω) of about 7×10^{-15} rad s^{-1} (Levshakov et al. 2016). In addition to L1251, only a few more filaments have been observed to show a velocity gradient along the filament minor axis, but in most cases, the gradients have been interpreted as being caused by accretion in a flattened structure, converging accretion flows or multiple components aligned in the line of sight, and not by rotation (Fernández-López et al. 2014; Beuther et al. 2015; Dhabal et al. 2018; Chen et al. 2020). Due to the difficulty in identifying filaments in line maps, the requirement of large high-sensitivity maps of an optically thin line with both high velocity and angular resolution, and the possible degeneracy in interpreting the complicated motion within a filament, precise measurements of the rotation and angular momentum of filaments are very rare.

In this paper, we present detailed measurements of the specific angular momentum of a star-forming filament. The area we studied, the HH24-26 low-mass star-forming region (a.k.a. LBS23) is a 1 pc long filament located in Orion B with a total mass around 230 $M_{\odot}$ and at a distance of approximately 400 pc (Lada et al. 1991; Lis et al. 1999). The large fraction of Class 0 protostars (∼50%) compared to the more evolved Class I, II, and III sources in this region (see Megeath et al. 2012; Furlan et al. 2016) suggest that LBS23 is a very young filament undergoing its first major phase of star formation.

In the following section (Section 2), we describe the observational data, the calibration, and the imaging process. In Section 3, we show the results of our observation. In Section 4, we analyze and discuss the stability of the rotating filament, as well as its dynamics and physical properties (density profile, turbulence, magnetic fields, specific angular momentum, and energy). In Section 5, we summarize the main findings and give our conclusions.

2. Observations

The results presented here come from Cycle 4 Atacama Large Millimeter/submillimeter Array (ALMA) observations of the LBS23 region (project ID: 2016.1.01338.S, PI: D. Mardones). The original goal of the project was to characterize the kinematics of gas and stellar feedback, over a range of scales, in a young filamentary cloud with active star formation. The observations were conducted using one spectral configuration (using ALMA Band 6) that simultaneously observed the 1.29 mm dust continuum emission and the following six molecular lines that trace different density and kinematic regimes: ^{12}CO(2–1), ^{13}CO(2–1), C^{18}O(2–1), $H_2CO(3_{0,3}$-$2_{0,2})$, SiO(5–4), and N_2D^+ (3–2). In this paper, we concentrate on the N_2D^+ (3–2) line (with a rest frequency of 231.32 GHz), the highest-density tracer in our spectral setup, as it clearly shows the most complete structure of the high-density narrow filament in the LBS23 region. Deuterated molecules such as N_2D^+ trace cold and dense gas, and thus it is a good tracer of dense structures like cores and filaments (Friesen et al. 2010; Kong et al. 2015, 2017). Other lines, which trace the more diffuse ambient gas, the outflows, and their impact on the cloud, will be presented in future papers.

We used two mosaic fields to cover the area of interest. The northern field is 220″ by 110″ and it is centered at $05^h46^m08^s.16$, $-00°10'58''.80$ (J2000). The southern field is 150″ by 110″ and is centered at $05^h46^m06^s.00$, $-00°13'49''.80$ (J2000). In total, these two fields encompass an area of about 360″ by 110″, which was observed using the ALMA 12 m, 7 m, and total power (TP) arrays.

To cover the northern field, we used 116 pointings with the 12 m array in the C34-1 configuration and 42 pointings with the 7 m array between 2017 March 26 and 2017 April 28. We used J0750+1231 as the calibrator for bandpass and flux calibration and J0552+0313 for phase calibration of the 12 m array visibility data. The total on-source integration time of the 12 m array, made with two executions, was 69 minutes and sampled a baseline ranging between approximately 15 and 390 m. The 7 m array observations, which were made with 10 executions with a total on-source integration of 141 minutes, used J0522-3627 for bandpass and flux calibration and J0532+0732 for phase calibration. The baseline coverage was from about 7 m to 49 m.

For the southern field, we observed 84 pointings with the 12 m array and 32 pointings with the 7 m array between 2017 March 22 and 2017 April 16. For the 12 m array observation, the baseline ranged from about 15 m to 161 m, and two executions provided a total on-source time of around 54 minutes. As for the 7 m array observations, the total on-source time was 70 minutes (provided by seven different executions), and employed baselines ranging between about 9 and 49 m. The southern field observations used the same calibrators as the northern field observations mentioned above. For both fields, we utilized the ALMA pipeline in the Common Astronomy Software Applications (CASA) version 5.4.0–70 to calibrate the data.

The northern and southern regions were observed with the total power array between late March and early July of 2017. The northern region was mapped with 2 to 4 antennas operated as single-dish telescopes with 26 executions, and the total on-source time was about 25 hr. As for the southern region, it was mapped with 3 to 4 TP antennas with 16 executions, and the total on-source time was about 17 hr. The TP array data exhibit a deep telluric absorption feature near the N_2D^+ line, which hampers the ability of the CASA pipeline to do a proper baseline subtraction. We therefore conducted our own baseline subtraction by fitting the baseline within ±20 km s^{-1} of the N_2D^+ line and at frequencies higher than the atmospheric absorption peak with a second-degree polynomial.

To recover the extended emission as much as possible, we used the properly baseline-subtracted total power map as both a start model and a mask when imaging the interferometry data using the CASA task *tclean*. We used the multi-scale deconvolver with scales of 0, 1, 3 beam sizes to recover flux at different scales, and natural weighting was applied to achieve the highest possible signal-to-noise ratio. To obtain a uniform synthesized beam across the entire area covered, we restricted the UV data to include baselines of up to 158 m for both fields. We used the CASA task FEATHER to combine the 12 m and 7 m array (interferometer) data with the total power data. The resulting map has a beam of $2\farcs66 \times 1\farcs61$ (P.A. $= -64.74°$) with an rms noise level of 32 mJy beam^{-1} per channel and a velocity resolution of 0.08 km s^{-1}.

The 1.29 mm continuum dust emission was observed (with bandwidth of 1875 MHz) simultaneously with the N_2D^+ line and calibrated using the same pipeline. Interactive cleaning with natural weighting was used for imaging the combined 12 m and 7 m array data, resulting in a dust continuum map with a synthesized beam of $2\farcs64 \times 1\farcs58$ (P.A. $= -64.80°$) and an rms noise level of 0.54 mJy beam^{-1}.

3. Results

The N_2D^+ integrated intensity map is shown in Figure 1(a). Most of the emission is concentrated in filamentary structures elongated along the north–south direction. We identify three different regions: the north, central, and south regions. In Figure 1(b), these are separated by thick horizontal blue lines and denoted as N, C, and S. The previously known young stellar objects in this area are also shown in Figure 1(b). The maps of the system velocity and velocity dispersion are shown in Figure 2.

The northern region includes a filamentary structure with a length of 65″ (0.13 pc), traced by the N_2D^+, as well as four young stellar objects. The N_2D^+ filament is wider in the north (where it coincides with continuum dust emission detected in our ALMA observations), and in the southern part, the structure narrows and bends toward the east. The four YSOs in this region have been identified as Class I and Class II sources (which are more evolved than the sources in the other two regions to the south). Three of the sources coincide with our detected continuum emission. However, unlike the other two regions to the south, none of the YSOs overlap with the N_2D^+ emission (as expected for more evolved YSOs). The CO(2–1) data (not shown here) reveal several outflows in this region, extending at least 0.1 pc, which are very likely interacting with the dense gas traced by the N_2D^+. The evolutionary stage of the sources, as well as the widespread outflow activity in the north region, suggest that this is the most evolved region of the three.

The main structure of the central region is an N_2D^+ filament with a length of 85″ (0.16pc). In the northern end of the filament, we find three very young protostars: the known Class 0 protostars HOPS 317 (Furlan et al. 2016) and HH24mms (Chini et al. 1993; Ward-Thompson et al. 1995), and a new source about 10″ (4000 au) northwest of the other two sources, which we name HH24mms-NW (see Figure 3(b)). Each of these protostars power their own compact outflow (extending only up to ∼0.05 pc from its source) traced by high-velocity CO and H_2CO emission, which may be impacting the immediate surroundings of the protostar, but certainly not the filament as a whole. The southern part of the central N_2D^+ filament (between decl. of about −0:11:40 and −0:12:00) is coincident with two continuum emission peaks (see Figure 3(b)). Compact high-velocity CO and H_2CO outflow emission within 0.02 pc of these continuum sources suggest that at least one of these harbors a very young protostar.

In the southern region, the N_2D^+ emission is composed of three condensations at around decl. = −0:12:15, a filament with a length of 105″ that extends to the south, and an isolated condensation in the southwestern edge of our map. Both the eastern and central N_2D^+ condensations at a decl. of about −0:12:15 harbor a Class 0 protostar (HOPS 402 and HOPS 401, respectively, see Figure 1(b)). The southern filament is home to two known Class 0 protostars, HOPS 316 and HOPS 358 (a.k.a., HH25mms), and to a number of previously undetected sources that we will present in a forthcoming paper. South of the filament lies the flat-spectrum source HOPS 385 and the Class I source HOPS 315, which is coincident with the southwestern condensation. Several of the protostellar sources in the southern region power high-velocity outflow lobes seen in our (yet to be published) CO ALMA data that extend about 0.1 pc from their driving source and are clearly interacting with the filament.

The elongated structures in these three regions have lengths ranging from 0.13 pc to 0.20 pc, and widths from about 0.01 to 0.04 pc. Therefore, these structures are significantly smaller than the typical star-forming filaments observed in dust continuum with the Herschel Space Observatory, which have lengths of about one to several tens of pc and widths of about 0.1 pc (André et al. 2014; Arzoumanian et al. 2019). The filamentary structures we detect are more similar in scale to the significantly narrower filaments mapped in the Orion A molecular cloud using high-resolution molecular line observations, like the narrowest $C^{18}O$ filaments reported by Suri et al. (2019), and the so-called fibers observed by Hacar et al. (2018) using N_2H^+.

In this paper, we will focus on the central region because of its comparative simplicity, significantly lower stellar feedback activity, and the relative young age of the filament and the sources in it. The quiescent central region is a good laboratory for studying the initial conditions for filament and core formation, while the south and north regions, which are more evolved and active, are more appropriate for studying how stellar feedback impacts cluster star formation in a filament (which will be discussed in detail in a future paper).

To highlight the structure of the filaments, we plot the peak intensity of N_2D^+ emission (Moment 8) in Figure 1(b). The central filament shows its brightest peak intensity in the northern half. However, close to the northern end of the central filament, we can see a clear attenuation of N_2D^+ emission at the position of the highest-intensity continuum peak (HH24mms). This is possibly due to the increase in temperature around this protostellar source, as N_2D^+ mainly traces low-temperature regions (Pagani et al. 2007; Kong et al. 2015, 2018). South of HH24mms, the filament shows local maxima in the N_2D^+ Moment 8 maps at the edges of the filament, around decl. −0:11:00. Further south, at around decl. −0:11:20, the central filament is significantly narrower and the intensity profile is centrally peaked.

In Figure 2, we present a velocity map derived from the N_2D^+ emission of the entire region, and in Figure 3, we zoom in on the central filament. To produce these maps and those of velocity dispersion (also shown in Figures 2 and 3), we

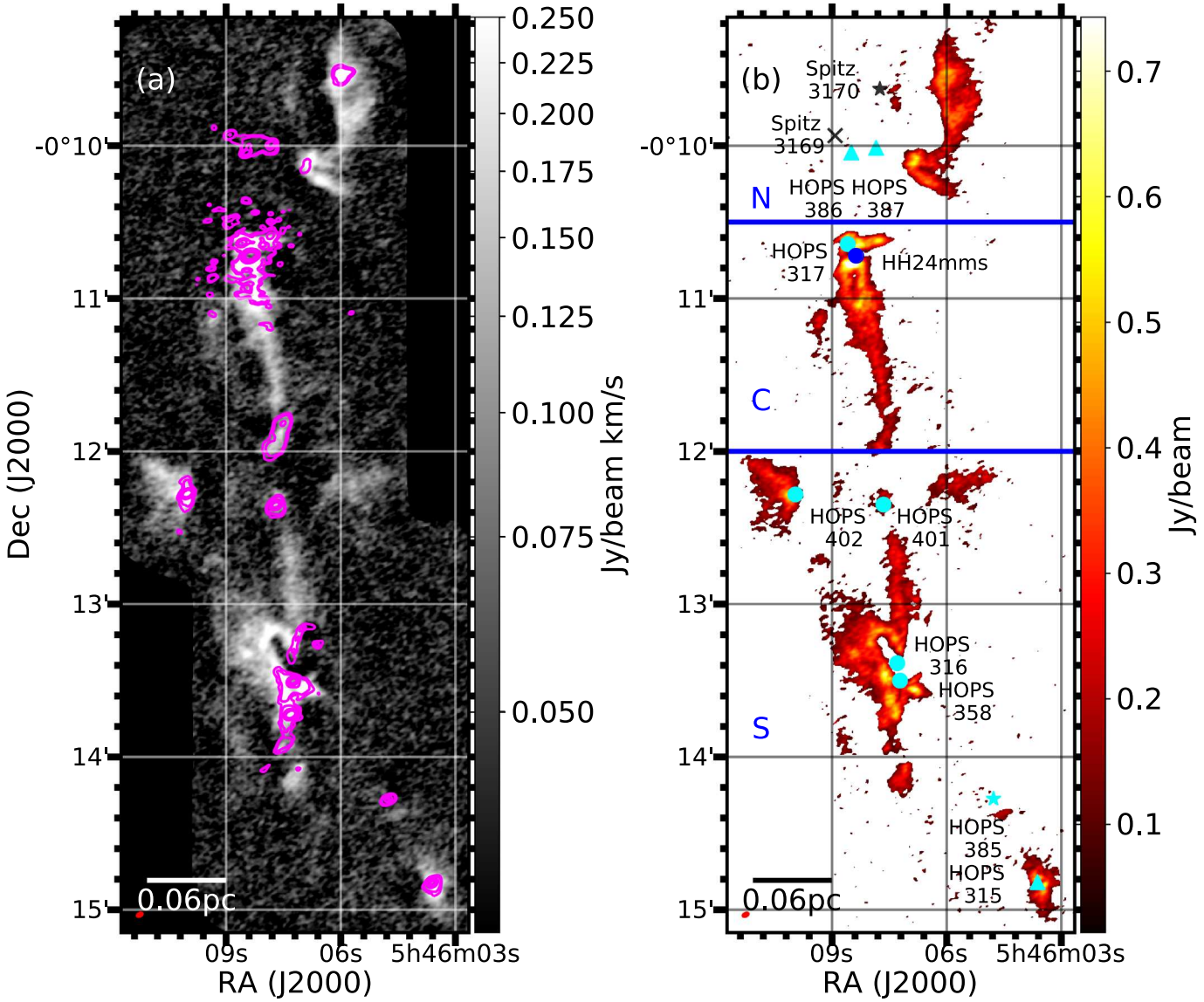

Figure 1. ALMA N_2D^+ $J = 3 - 2$ maps of the LBS23 region. (a) Integrated intensity map of the N_2D^+ emission. Magenta contours represent the 1.29 mm dust continuum emission in steps of 3σ, 5σ, 20σ, 40σ, 80σ, 320σ, where $\sigma = 5.4 \times 10^{-4}$ Jy beam^{-1}. (b) N_2D^+ peak intensity (Moment 8) map. Previously known sources are shown. HOPS Class 0, Class I, and flat-spectrum sources are marked by cyan circles, cyan triangles, and cyan stars, respectively (Furlan et al. 2016). Spitzer-identified pre-main-sequence star and red protostar (detection in 24 μm without detection in 4.5, 5.8, or 8 μm) are marked as a black star and cross, respectively (Megeath et al. 2012). Blue circle marks the position of the Class 0 protostar, HH24 mms. Northern, central, and southern regions are identified with the letters N, C, and S, respectively, and separated by thick blue horizontal lines. Size of the synthesized beam is represented with a red ellipse in the lower left corner of each panel.

modeled the brightest 25 hyperfine lines of the N_2D^+(3–2) transition listed in Table 2 of Gerin et al. (2001) with 25 Gaussians, using the known relative frequencies and intensities of the hyperfine lines, and assuming the emission is optically thin.

In Figures 2(a) and 3(a), it can be seen that there is an east–west velocity gradient across approximately the entire length of the central filament. In addition, the north part of the southern filament appears to show a velocity gradient similar to that of the central filament (see Figure 2(a)). It is possible that these two filaments were once connected and their kinematics had the same origin. The protostar HOPS 401 lies between these two filaments, and its formation could have resulted in the current disconnect between the central and southern structures. Although our observations cannot confirm this scenario, what is apparent from our data is that these two filaments are now disconnected, and as such we will assume they are independent structures.

The velocity in the central filament gradient is purely along its minor axis with no detectable gradient along the length (major axis) of the filament. This implies that either there is little or almost no gas following along the filament or the filament lies mostly on the plane of sky. From the channel maps shown in Figure 4, we can see the position of the filament changes from east to west, as a whole, as the V_{lsr} increases, with no noticeable velocity structure alone the length of the filament. As most filaments show some velocity structure along their major axis (e.g., André et al. 2014), this suggests that the central N_2D^+ filament has little or almost no inclination with respect to the plane of the sky.

In Figure 3(b), we show the N_2D^+ linewidth map. It can be seen that the linewidth mostly ranges between 0.15 and 0.35 km s^{-1}. Local maxima coincide, for the most part, with

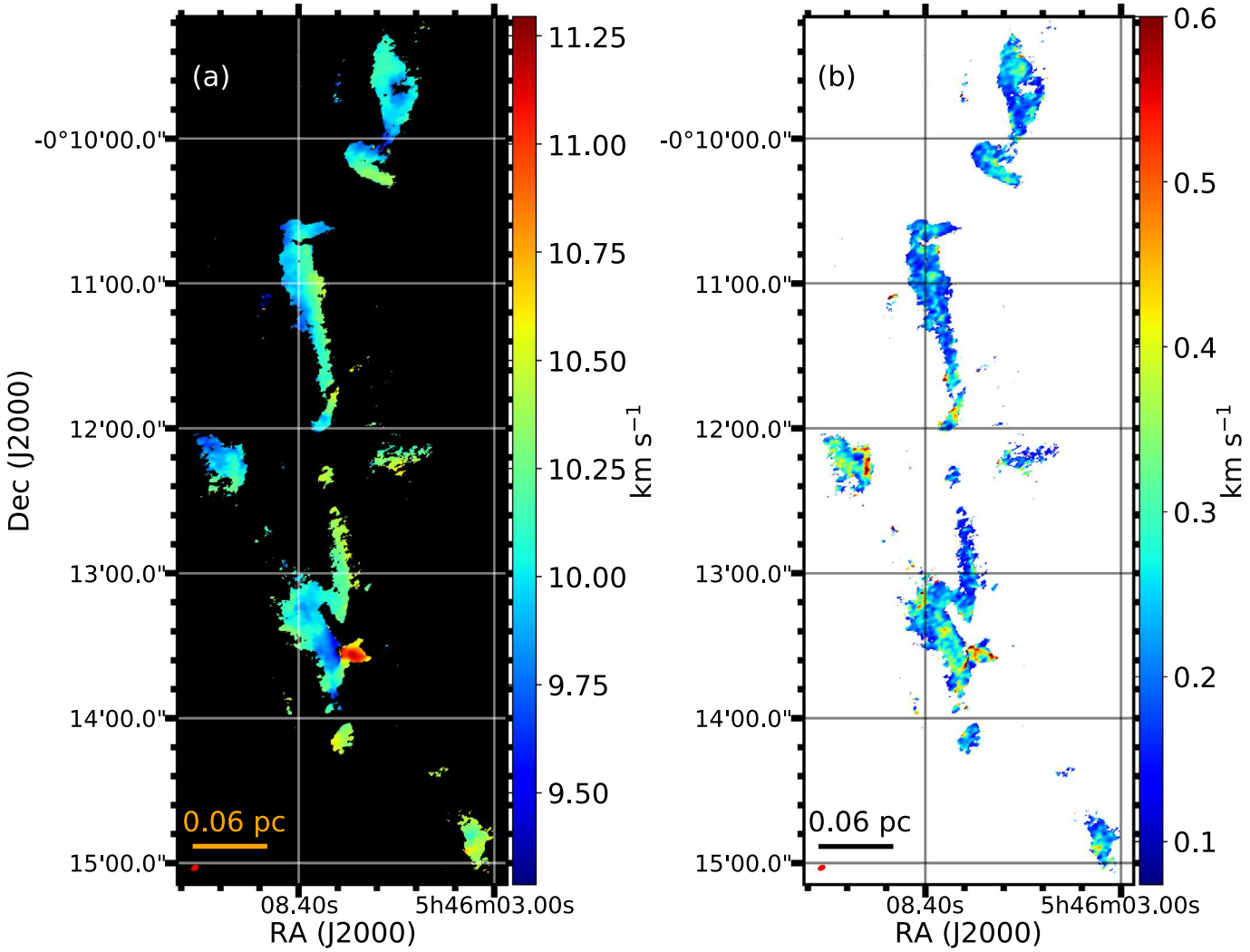

Figure 2. Kinematics of the entire LBS23 region from fits to the N_2D^+ hyperfine line emission. (a) System velocity map. (b) Velocity dispersion map. Beam is shown as a filled red ellipse in the lower left corner of each panel.

continuum peaks that trace prestellar and protostellar envelopes. In these regions, the increase in linewidth is likely due to unresolved motions surrounding these sources, such as outflows and infall. Between −0:11:00 and −0:11:20, we also see a local maximum of linewidth along the spine and toward the eastern edge of the filament, and south of −0:11:20, the linewidth is higher toward the edges. In summary, there is no ordered structure in the linewidth map across the entire filament as there is in the velocity map.

In principle, we could use the N_2D^+ emission to derive the N_2D^+ column density and obtain an estimate of the total filament mass. However, vast variations in the deuterium-to-hydrogen abundance ratio in clouds and cores can yield N_2D^+ abundance ratios that range a few orders of magnitude (Caselli et al. 2002; Linsky et al. 2006; Lique et al. 2015). Therefore, mass estimates from measurements of the N_2D^+ column density, assuming a constant abundance ratio of N_2D^+ to H_2, are highly uncertain. Here, instead, we use the 850 μm Herschel-Plank dust emission map (from Lombardi et al. 2014) in concert with our ALMA data to estimate the H_2 column density and N_2D^+ abundance of the central filament (see Appendix A).

To convert H_2 column density to number density, we assumed a cylindrical filament and that the average depth of the filament (the dimension along the line of sight) is equal to the radius multiplied by $\frac{\pi}{2}$ (i.e., the area of a circle divided by its diameter). The central filament has dimensions (as seen on the plane of the sky) of $13\farcs8 \times 87\farcs6$ (5540 × 16640 au).[6] We thus estimate the peak and average number density for the central filament to be approximately 6.6×10^6 cm^{-3} and 1.6×10^6 cm^{-3}, respectively. We sum the column density within the area of the filament to obtain the total filament mass of 11.7 $M_\odot$, which corresponds to a linear mass of 64.6 $M_\odot$ pc^{-1}. We estimate an approximate 50% uncertainty in our calculation of the filament mass, which results from the error in the fit to the empirical relation between the N_2D^+ integrated intensity and the H_2 column density (see Appendix A) and the range of mass estimates obtained when choosing a range of thresholds for the minimum signal-to-noise emission that is used for determining the mass.

[6] Note that the filament width varies (it becomes narrower toward the south; see Figure 3). For all the number density and mass calculations, we use the average width of $13\farcs8$ (5540 au), estimated from the Moment 0 map where only emission above 4σ is included.

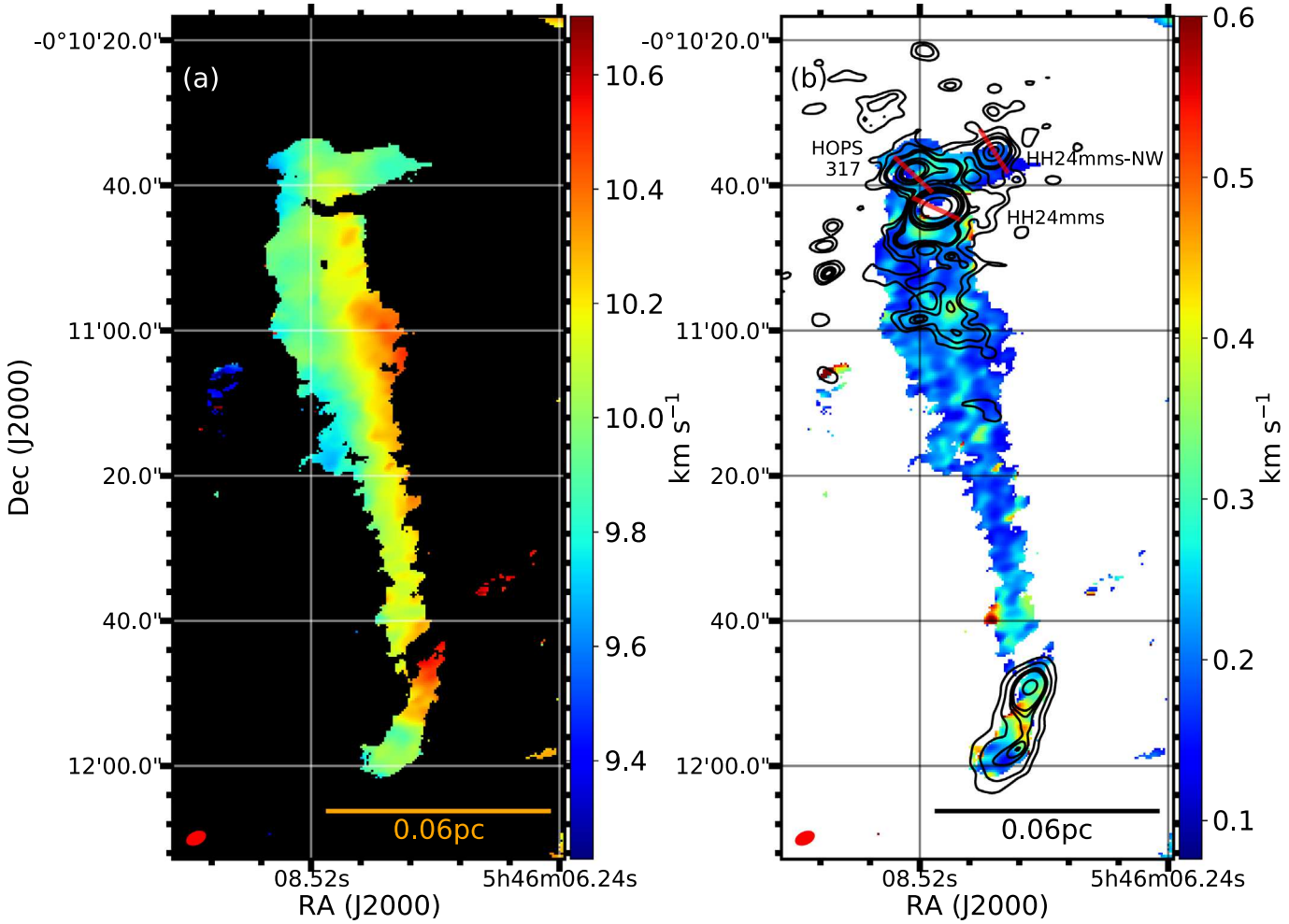

Figure 3. Kinematics in the central filament in LBS23. These panels are zoomed-in versions of the panels in Figure 2 (with a different color scale). (a) System velocity map. (b) Velocity dispersion map. Black contours in panel (b) show the 1.29 mm dust continuum emission in steps of 3σ, 5σ, 7σ, 9σ, 10σ, 20σ, 40σ, 80σ, 320σ, where $\sigma = 5.4 \times 10^{-4}$ Jy beam^{-1}. Red lines mark the direction of the outflows powered by the three protostars identified in the northern edge of the filament. Size of the synthesized beam is represented with a red ellipse in the lower left corner of each panel.

Assuming this is an isothermal filament with a temperature of 10 K, we use Equation (59) in Ostriker (1964) to estimate the critical mass per unit length[7] (for a nonrotating filament) to be $M_{\rm line,crit} \sim 25.2\ M_\odot\,{\rm pc}^{-1}$. This is lower than the estimated linear mass for the central filament, which indicates that the filament is gravitationally unstable. As we discuss below, the central filament in LBS23 is rotating and this should be considered in the stability analysis of this filament. That is what we do in the following section.

4. Discussion

4.1. Rotation and Its Effect on Filament Dynamics

In Figure 2(a), we observed a clear velocity gradient along the minor axis of the central filament. To further study this kinematic structure, we plot the average velocity profile across the filament in Figure 5. Here, we see a clear increase in radial velocity from east to west across the central filament. We interpret this gradient to be caused by rotation in the filament (see Section 4.6 for a discussion on this), and use the velocity profile to estimate the rotation velocity. In Figure 5, we see that the velocity increases from about 9.8 km s^{-1} in the eastern edge of the filament to 10.4 km s^{-1} in the west. The rotation velocity is determined to be half of the total velocity range of the filament, or about 0.3 km s^{-1}. Dividing the presumed circumference of the cylinder by the rotation velocity, we estimate the rotation period ($T = \frac{2\pi r}{v}$, where $\frac{v}{r} = 20 \pm 1\,{\rm km\,s\,pc}^{-1}$) to be 3.1×10^5 years, which corresponds to an angular frequency (ω) of $6.5 \pm 0.3 \times 10^{-13}$ rad s^{-1}.

To further analyze the dynamics of the filament, we compare our results with the theoretical study of Recchi et al. (2014), which considers a rotating filament model in hydrostatic equilibrium. Following Recchi et al., we calculate the normalized angular frequency[8] (Ω) for the central filament to be 0.36. To obtain this value, we used a central density (ρ_0) of about 3.0×10^{-17} g cm^{-3} (obtained from the estimate of the number density given above). If the centrifugal force balances the gravitational force (i.e., $\Omega = 2.0$), then the filament would be in Keplerian rotation and would have a constant density profile

[7] The equation for the critical mass per unit length is: $M(x) = \frac{2kT}{\mu m_p G}\left(1 + \frac{1}{x^2}\right)^{-1}$, where x is the dimensionless width shown in Recchi et al. (2014). In our case, $x = 3$ (see Section 4.1). The commonly used value in the literature of $M_{\rm line,crit} \sim 16\ M_\odot\,{\rm pc}^{-1}$ results from the assumption of much larger filament widths, with $x \to \infty$ (e.g., André et al. 2014).

[8] $\Omega = \omega\sqrt{2/\pi G\rho_0}$, where ρ_0 is the central density.

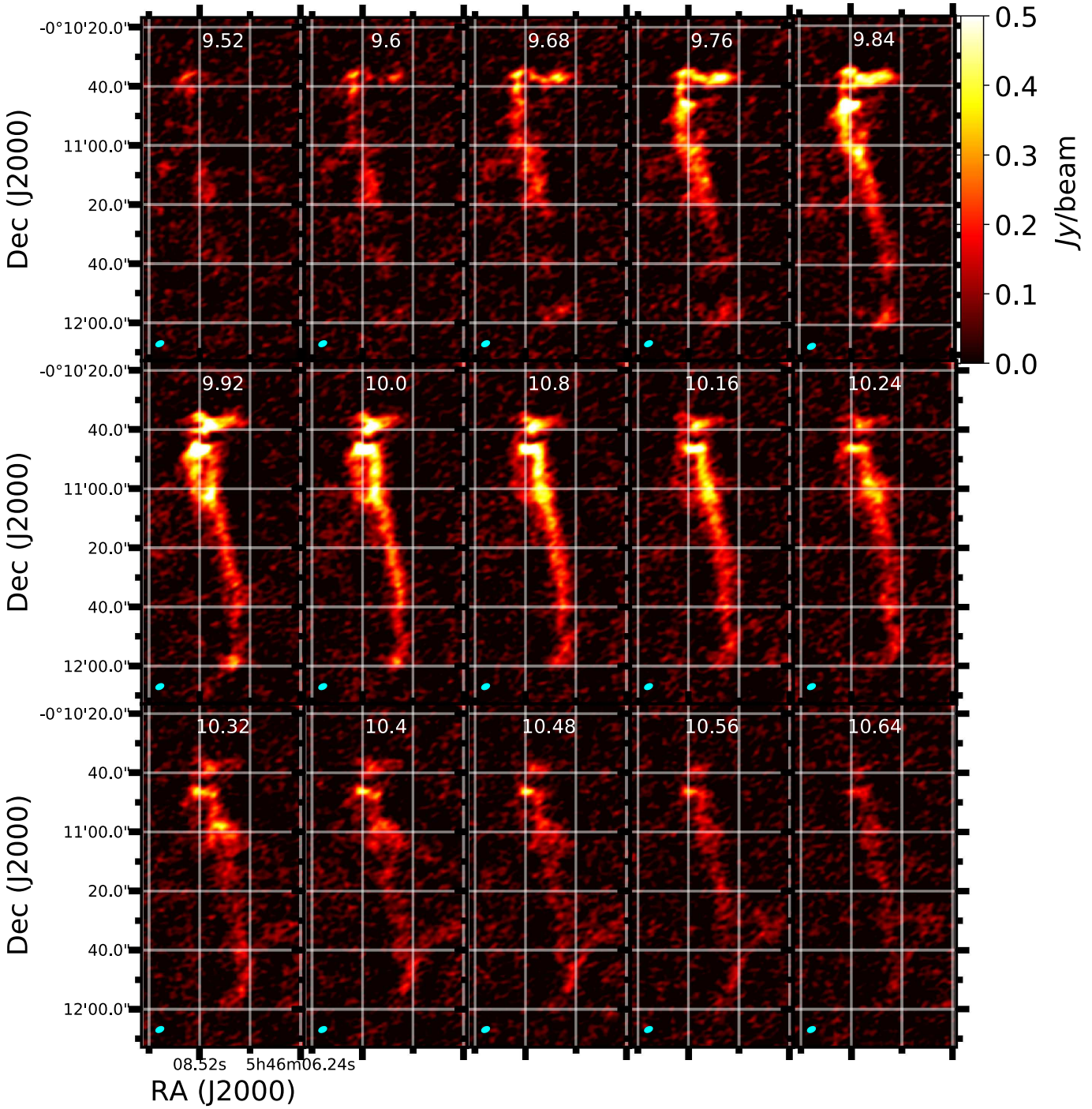

Figure 4. Channel maps of the N_2D^+ ($J = 3 - 2$) emission of the central filament. The V_{lsr} of each channel is shown at the top of each panel. Cyan ellipse in the lower left corner of each panel shows the beam size of the N_2D^+ map.

(Inagaki & Hachisu 1978; Recchi et al. 2014). In our case, $\Omega < 2.0$ and thus the centrifugal force is less than the gravitational force. Using our estimate of the central density and assuming a temperature of 10 K, we estimate the dimensionless truncation radius (x).[9] Assuming the filament is isothermal, and using the same theoretical calculation as that used to obtain the values of Table 1 in Recchi et al. (2014), we find the critical linear mass ($M_{\rm line,crit}$) for an isothermal rotating filament with truncation radius of $x = 3.0$ and normalized angular frequency of ~0.36 is 29.0 $M_\odot$ pc^{-1}. This value is slightly larger than the critical linear mass for an isothermal 10 K nonrotating cylinder (Ostriker 1964; Inutsuka & Miyama 1997). Our results show that the central filament has a linear mass that is significantly higher than the critical linear mass (even after taking rotation into account), and thus the filament is not stable against collapse. This is consistent with the evidence of fragmentation observed in the continuum emission and protostellar activity in both the northern and southern edge of the central filament (see Section 3).

[9] $x = r/\sqrt{\frac{2kT_0}{\pi G \rho_0 \mu m_H}}$, where T_0 is the central temperature (see Recchi et al. 2014).

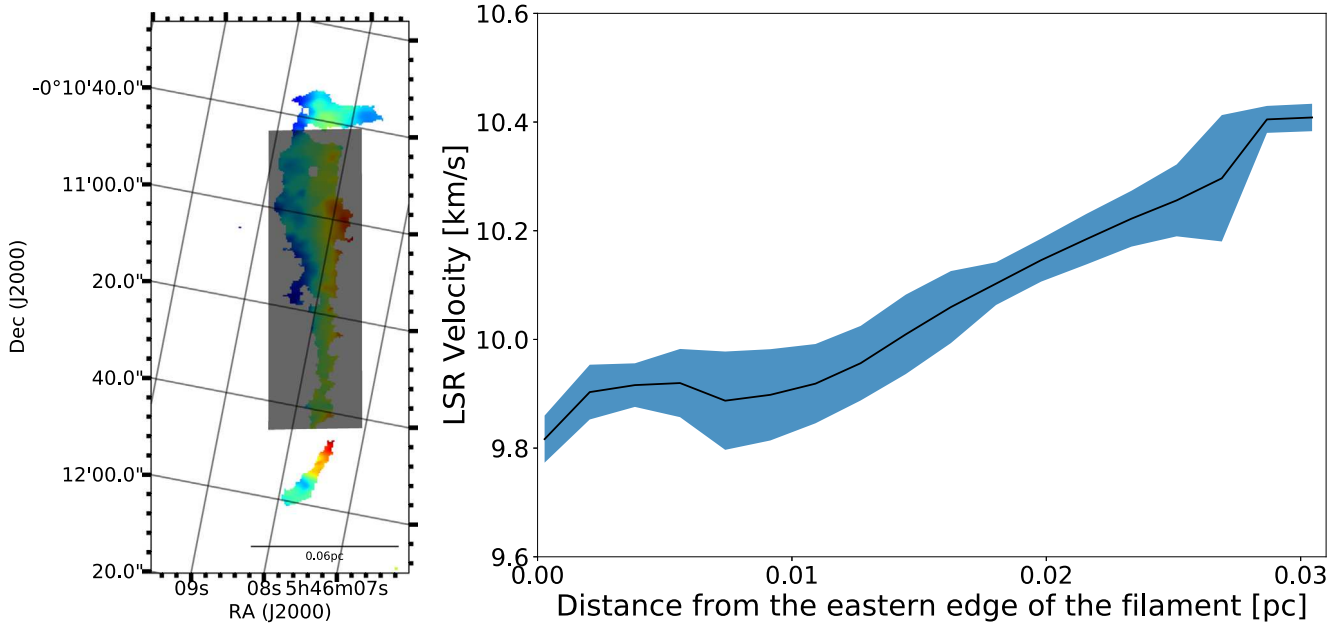

Figure 5. N_2D^+ system velocity profile across the central filament. Left panel shows the velocity map (from Figure 2(a)) and the area from which the average velocity profile along the filament minor axis, shown in the right panel, was obtained. Figure has been rotated by 11° (north of east) in order to have the filament's long axis parallel to the *y*-axis of the plot. Black line in the right panel represents the average velocity profile. Blue region surrounding the black line in the right panel represents the standard deviation around the average.

To further understand the importance of rotation in the filament's dynamics, we calculate $\beta_{\rm rot}$, the ratio between rotational kinetic energy to gravitational energy (see Appendix C for a detailed description of how we calculated these quantities). We obtain a value of $\beta_{\rm rot} \sim 0.04$ for the central filament in LBS 23. This value is consistent with our result that the central filament is not stable against collapse, even when considering rotation. Our estimate of $\beta_{\rm rot}$ is similar to the average value obtained for cores by Goodman et al. (1993), and in agreement with the estimate of $\beta_{\rm rot}$ for the cores and envelopes with sizes similar to those of our filament listed by Chen et al. (2013). Even though the rotation in the filament is not enough to prevent collapse, it may still trigger the formation of instabilities (e.g., fragmentation, bars, rings). For example, the numerical simulations by Boss (1999) and Bate (2011) show that cores with $\beta_{\rm rot} \geqslant 0.01$ can form dense, flattened structures that may then fragment. These simulations modeled rotating molecular cloud cores, ergo their results may not be entirely applicable to filaments. Simulations of collapsing rotating filaments should be conducted to determine the importance of rotation in triggering fragmentation and the formation of other instabilities in filaments.

4.2. Specific Angular Momentum Profile of Filament

Various observational studies have measured the specific angular momentum in cores and envelopes, with scales from ~0.01 pc to about 0.1 pc (Goodman et al. 1998; Caselli et al. 2002; Tatematsu et al. 2016) and in early Class 0/I disks, with scales $\leqslant$100 au (Ohashi et al. 1997; Chen et al. 2007; Tobin et al. 2012; Kurono et al. 2013; Yen et al. 2015). Based on these measurements, it has been proposed that specific angular momentum is conserved from scales of the inner envelope (a few 10^3 au) to disk scales (~10–100 au) (Ohashi et al. 1997; Belloche 2013; Gaudel et al. 2020). In order to understand how angular momentum varies (or is conserved) at various scales, it is essential to obtain specific angular momentum measurements of different structures of different sizes (i.e., filaments, cores, envelopes, and disks). In this work, we concentrate on the filament scales.

We measure the specific angular momentum of the filament by assuming a rotating cylinder model. The specific angular momentum $J = L/M$ can be expressed as:

$$J = \frac{L}{M} = \frac{I\omega}{M}. \quad (1)$$

Using the angular frequency ω and radius r measured in Section 4.1 and the moment of inertia (I) calculated in Appendix C, we find the total specific angular momentum for the central filament to be $\sim 4 \pm 2 \times 10^{20}$ cm^2 s^{-1}.

Tatematsu et al. (2016) measured the total specific angular momentum of 27 N_2H^+ cores in Orion A using the Nobeyama 45 m radio telescope, and found that it ranges between about 10^{20} to 10^{21} cm^2 s^{-1} (see their Table 2). These cores have a typical size of approximately 0.04 pc to about 0.1pc, which is comparable to our N_2D^+ filament width of about 0.04 pc. N_2H^+ and N_2D^+ are both high-density tracers, and in the cold pre- or protostellar cores where CO freezes onto dust grains, the ratio N_2D^+/N_2H^+ is about 0.24 (Caselli et al. 2002). The near-unity abundance ratio, as well as the similarity of structures in maps of young cores using these species (e.g., Tobin et al. 2013), suggest that both species trace somewhat similar density regimes. The similarity in the specific angular momentum between cores and our filament may suggest that angular momentum of cores is linked to the rotation of small filaments.

Our observations have sufficient resolution to be able to determine how the specific angular momentum varies with distance from the center of the filament. In Figures 5 and 6, we plot the velocity profile and its derived specific angular momentum profile ($j(r)$), respectively, for the central N_2D^+ filament. The measured specific angular momentum as a function of radius is given by $j(r) = r \times V_{\rm rot}$, where r is the radius from the filament center (which in Figure 5 corresponds

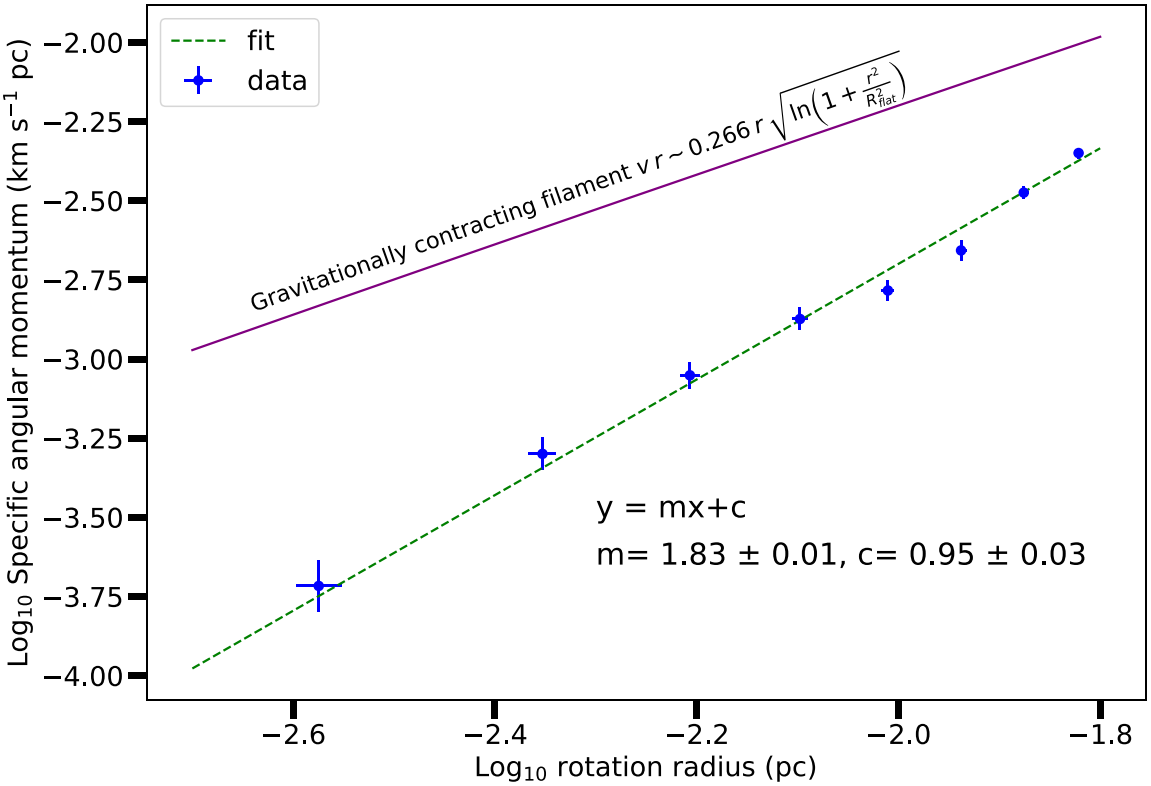

Figure 6. Radial profile of the specific angular momentum ($j = r \times V_{\rm rot}$) for the N_2D^+ filament, derived from the velocity profile shown in Figure 5. Blue points represent the average rotational velocity obtained by averaging the velocities at similar distances from the filament center on the eastern (blueshifted) side and the western (redshifted) side of the filament. Dotted green line shows the best-fit line to the data in log-log space. Purple line represents the expected $r \times v$ profile for a gravitationally contracting filament (see Section 4.6).

to 0.15 pc from the eastern edge of the filament), and $V_{\rm rot}$ is the rotational velocity around the filament's rotational axis. In our case, $V_{\rm rot} = |V(r) - V_c|$, where $V(r)$ is the $V_{\rm lsr}$ at radius r from the center of the filament, given by the plot in Figure 5, and V_c is the $V_{\rm lsr}$ at $r = 0$, which is 10.05 km s^{-1}.

A fit to the data (using $j(r) \propto r^{\alpha}$) gives an exponent of 1.83 ± 0.01 (see Figure 6). This is consistent with the relation of total specific angular momentum as a function of core radius ($J \propto R^{1.6\pm0.2}$) for a sample of cores derived by Goodman et al. (1993), as well as the results of more recent works that have obtained the average specific angular momentum profile of a sample of young protostars (Pineda et al. 2019; Gaudel et al. 2020).

The similarity in the angular momentum profile of our filament and that of the dense cores and envelopes suggests that the angular momentum of the dense circumstellar environments may be linked to (and even inherited from) the rotation of small filaments. One (naive) first step to determine whether such a link exist in the central filament in LBS23 is to compare the rotational axis of the envelopes surrounding the protostars in the filament with the rotational axis of the filament. The resolution of our observations is not enough to obtain a reliable rotational axis from the envelope emission. Instead, we use the outflow axis as a proxy for the envelope/disk rotation axis.

In Figure 3, we plot the outflow axes of the three protostars in the central filament of LBS23 with reliable outflow detection. Even though the outflow axes are clearly not aligned with the filament rotation axis, it would be too premature to conclude that there is no link between the filament and envelopes from this simple comparison. It could be that, although the outflows are tracing the spin axis of the circumstellar disk, it is not the same as that of the envelope (e.g., Bate 2018). In addition, given the small projected separation between the three protostars in the northern end of the filament (less than 4000 au), it is very likely that they are part of a (hierarchical) triple system (e.g., Chen et al. 2013; Tobin et al. 2016). If that is the case, then the total angular momentum of the system, which consists of the envelope spin and the orbital angular momentum of all members, is the quantity that should be associated with the specific angular momentum of the filament and not the spin of the individual members.

Studies suggest that the observed rotation in cores and envelopes, with a power-law dependence with an index of about 1.6, is produced by the turbulence cascade of their parent molecular cloud (Chen & Ostriker 2018; Gaudel et al. 2020). Our filament shows a similar dependence, and thus it is tempting to suggest that the velocity gradient seen along the minor axis of our filament is acquired from turbulence as well. In our filament, this power-law dependence is seen to continue down to our resolution level of about several 10^2 au. This is different from the observed flattening of the specific angular momentum as a function of radius (or size) at scales of a few 10^3 au in a sample of various young stellar systems (Ohashi et al. 1997; Belloche 2013; Li et al. 2014; Gaudel et al. 2020). This flattening is thought to indicate the scale for dynamical collapse, where angular momentum is conserved.

In the traditional two-step scenario where thermally supercritical filaments form first and cores then form via gravitational fragmentation (Ostriker 1964; Inutsuka & Miyama 1992, 1997), we would expect a clear transition between the angular momentum profile of the filament

(inherited from the cloud turbulence) with a power-law dependence and a flattening of the angular momentum profile at the core scales, where gravity dominates and angular momentum is conserved. In contrast to this scenario, our observed filament shows a profile that is consistent with a specific angular momentum profile set by turbulence all the way down to a few hundred au (scales that are even smaller than the size of the triple system at the northern end of the filament). Our observations are thus more consistent with the scenario in which filaments and cores develop simultaneously due to the multi-scale growth via nonlinear perturbation generated by turbulence; for more details, see the numerical simulation studies by Gong & Ostriker (2011, 2015), Chen & Ostriker (2014, 2015), Gómez & Vázquez-Semadeni (2014), and Van Loo et al. (2014). In this picture, the initial angular momentum of a filament and the cores inside it are first acquired from the ambient turbulence. Subsequent gravitational interactions among dense condensations may redistribute the angular momentum of individual cores and envelopes (as suggested by Kuznetsova et al. (2019)). This could also explain the difference in the outflow axes and the filament rotation axis.

4.3. Transonic Turbulence in the Filament

One general way to understand the properties of a filament is to characterize its turbulence. Previous observations of cores by Goodman et al. (1998) have shown that medium-density tracers such as $C^{18}O$ show supersonic velocity dispersion while denser tracers such as NH_3 show velocity width comparable to the thermal line width. Pineda et al. (2010) used NH_3 as a high-density tracer to study the B5 region in Perseus. They found a ~0.1 pc wide filamentary region with subsonic turbulence surrounded by supersonic turbulence. The subsonic coherent cores mark the point where most of the turbulence decays and the gas is ready to form protostars (Goodman et al. 1998; Caselli et al. 2002; André et al. 2013).

We measured the nonthermal motion in our filament using the following equation:

$$\sigma_{\rm NT} = \sqrt{{\sigma_v}^2 - \frac{k_{\rm B}\, T_g}{m_{N_2D^+}}}, \quad (2)$$

where σ_v is the observed velocity dispersion shown in Figure 3(b), $k_{\rm B}$ is the Boltzmann constant, T_g is the gas temperature, and $m_{N_2D^+}$ is the mass of the N_2D^+ molecule. From Figure 3(b), we can see the typical velocity dispersion along the line of sight ranges from about 0.15 to 0.35 km s^{-1}. The velocity dispersion is greater in the regions with evidence of protostellar activity, close to the positions of the continuum sources in the northern and southern edges of the filament. We find the average velocity dispersion within the area (chosen to avoid outflow "contamination") south of HH24mms and north of the continuum peaks in the southern end of the central filament to be 0.20 km s^{-1}. Assuming a temperature of 10 K, the sound speed ($c_s = \sqrt{k_{\rm B} T_g/\mu m_H}$, where $\mu = 2.33$ is the mean molecular weight, and m_H is the mass of the hydrogen atom) is around 0.19 km s^{-1}. Thus, the average nonthermal velocity component is estimated to be ~0.19 km s^{-1}, resulting in an average Mach number (M_s) of 1.0 for the central filament. This is in contrast with the subsonic turbulence ($M_s < 1$) that is generally expected for dense structures with scales less than 0.1 pc, as well as the picture of coherent cores (Goodman et al. 1998; Caselli et al. 2002). However, our finding is consistent with recent observations of a few star-forming filaments/fibers with transonic turbulence (Friesen et al. 2016; Hacar et al. 2017). The existence of young protostars in a transonic filament, as is the case in the central filament of LBS23, suggests that star formation can occur before the turbulence fully decays from supersonic to subsonic.

Table 1
Estimated Energies for the Central Filament

Energy Type	Value (erg)	Ratio ($1/E_G$)
Gravitational Energy (E_G)	7.1×10^{43}	1.0
Turbulence Energy (E_σ)	9.7×10^{42}	0.14
Rotational Energy (E_R)	3.0×10^{42}	0.05
Magnetic Field Energy ($E_{\rm B}$)	3.4×10^{43}	0.48

In order to assess the relative importance of turbulence, we estimated the turbulence energy of the central filament, using

$$E_\sigma = M\sigma_{\rm NT}^2, \quad (3)$$

where $\sigma_{\rm NT}$ is the nonthermal velocity dispersion, and M is the mass of the central filament (Fiege & Pudritz 2000). Using our estimates for these two quantities, we obtain a turbulence energy of 9.7×10^{42} erg, with a ratio of turbulence to gravitational energy of 0.14 (see Table 1). A significantly lower value of the turbulence energy compared to the gravitational energy should be expected in a dense region where protostars are forming.

The turbulence energy in the central filament is about a factor of three larger than the rotational energy ($E_{\rm rot}$). Protostellar cores and envelopes with velocity gradients indicative of rotation generally have rotational energy that are significantly smaller than the turbulence energy. This can be clearly seen in the results of Chen et al. (2007), who studied a sample of protostellar envelopes, traced by the N_2H^+ emission. In addition, the study of Tatematsu et al. (2016) found that, for a typical core in Orion, the average velocity gradient, presumably due to rotation, is 2.4 ± 1.6 km s^{-1} pc^{-1} and the average core diameter is 0.08 ± 0.03 pc. Therefore, the average rotation velocity is estimated to be ~0.19 km s^{-1}. A large survey of 71 cold cores in Taurus, California, and Perseus found an average nonthermal velocity width of ~0.3 km s^{-1} (Meng et al. 2013). Thus, we expect that cores will have $E_\sigma / E_{\rm rot} \approx \left(\frac{0.3}{0.19}\right)^2 \approx 2.5$; consistent with our results for the central filament in LBS 23. Even thought the rotational energy is relatively small, rotation can still have an impact on the kinematics and structure of the system (see Section 4.1).

We investigate whether this level of turbulence can be maintained in the filament, as well as how it will evolve. To do this, we first estimate the turbulence dissipation rate, given by $L_\sigma = E_\sigma / t_{\rm diss}$ (e.g., Arce et al. 2011). The turbulence dissipation timescale (t_{diss}) is given by $t_{\rm diss} = \eta t_{ff}$, where t_{ff} is the freefall time and η ranges between ~1 and 10 (McKee 1989; Mac Low 1999). Pon et al. (2012) estimated the uniform cylinder collapse time ($t_{ff,\rm cylinder}$) to be $t_{ff,\rm cylinder} = \sqrt{\frac{2}{3}} A t_{ff,\rm sphere}$. Here, A is the aspect ratio of the cylinder, which for our case is approximately 6, and $t_{ff,\rm sphere}$ is the classical freefall timescale of a uniform-density sphere with the same volume density as the cylinder. Adopting $\eta = 5$ and the average H_2 number density of the filament 1.56×10^6

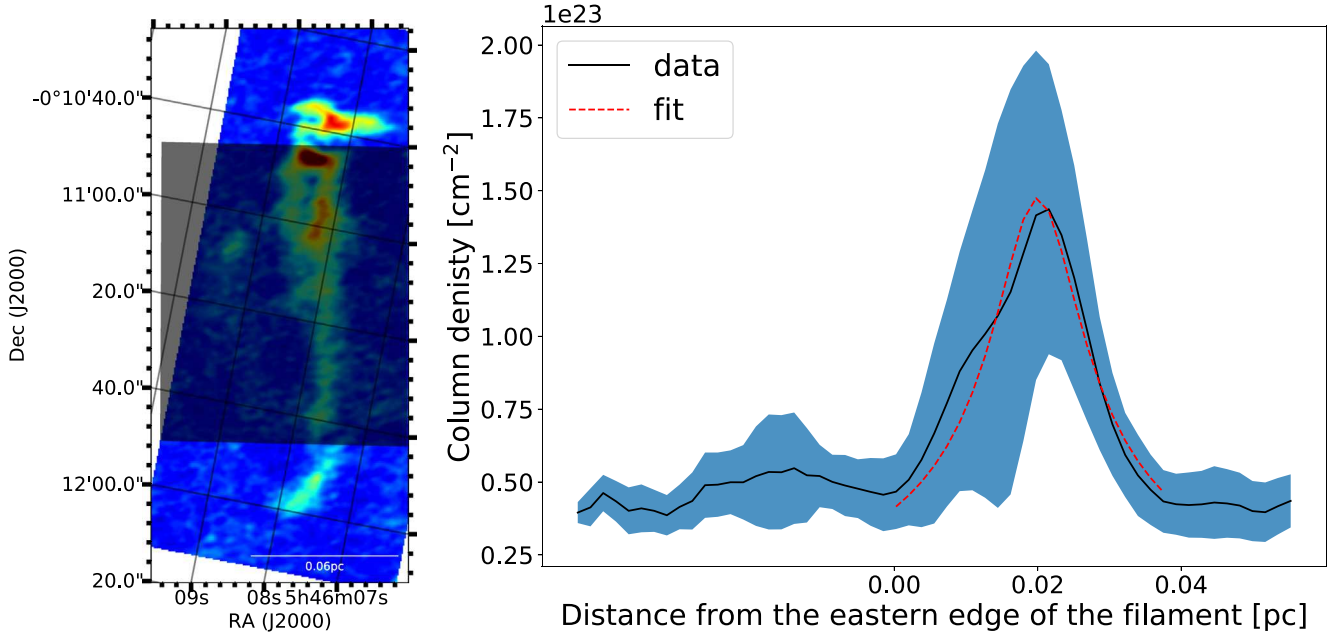

Figure 7. H_2 column density profile of the central filament in LBS23. Left panel shows the N_2D^+ column density map (see Appendix B). The 0.18 pc long shaded area shows the region from which we obtain the average column density profile. Figure has been rotated by 11° (north of east) in order to have the filament's long axis parallel to the *y*-axis of the plot. Black line in the right panel shows the average N_2D^+ column density, and the blue shade surrounding it represents the standard deviation around the average. Dotted red line represents the best fit to the Plummer profile (see Equation (4) and Section 4.4).

cm^{-3} (see Section 3), we find the freefall time for our filament to be 1.9×10^5 yr, which leads to a turbulence dissipation rate of 3.3×10^{29} erg s^{-1} for the central filament. Feddersen et al. (2020) observed 45 protostellar outflows in Orion A, and found the kinetic energy injection rates of outflows are comparable to the turbulent dissipation rate. The energy ejection rate of outflows in Orion A ranges from about 10^{30} to a few 10^{32} erg s^{-1} (Feddersen et al. 2020). If we assume that the four outflows in the filament have energy injection rates similar to those in Orion A, then these protostellar outflows have more than enough power to maintain the turbulence in the filament, even if we were to assume a low efficiency in the coupling between outflow energy and filament turbulence. The excess outflow energy ejection rate could eventually increase the turbulence energy in the filament and prevent it from further collapse.

4.4. Filament Density Profile

Another property that is commonly determined from observations is the filament density profile, as it may provide information regarding the dynamical stability of the filament and its formation. In Figure 7, we show the column density profile perpendicular to the central filament averaged over a 0.18 pc long region along the filament length. We then fit the average column density profile with a Plummer-like profile:

$$N(r) = \frac{N_0}{\left[\left(1 + \left(\frac{r}{R_{\rm flat}}\right)^2\right)\right]^{(p-1)/2}}. \quad (4)$$

The fit gives values for the power-law index (p) of 2.1 ± 0.2, the central (peak) column density (N_0) of $1.48 \pm 0.09 \times 10^{23}$ cm^{-2}, and the radius of the inner flat region (R_{flat}) of 0.006 ± 0.002 pc. The value of p we obtain for the central filament is significantly lower than the steep power-law index of $p = 4$ expected for an isothermal nonrotating cylinder in hydrostatic equilibrium (Ostriker 1964). On the other hand, our result for the central filament in LBS23 is consistent with observations of filaments of various sizes (Arzoumanian et al. 2011, 2019; Palmeirim et al. 2013; Kainulainen et al. 2016) as well as hydrodynamic and MHD simulations (Gómez & Vázquez-Semadeni 2014; Smith et al. 2014; Federrath 2016) of clouds which show that filament column density profiles can be well-fitted with a Plummer-like profile with $p \sim 2$. Federrath (2016) argues that such a density profile can be explained by filaments formed in the collision of two planar shocks in a turbulent medium, as the structure formed from this collision is expected to have a density profile that scales as r^{-2}, which corresponds to $p = 2$.

4.5. Magnetic Fields in the LBS 23 Filament

For a rotating system, the magnetic braking effect can quickly slow down rotation, and this has been found to be one of the challenges in disk formation theories (Li et al. 2011). If the rotating filament is threaded by magnetic fields, the magnetic tension could slow down the rotation. To study the magnetic fields in the LBS 23 filament, we use the archival 850 μm SCUBA polarimeter data (with a beam of $\sim$20″) from the James Clerk Maxwell Telescope (JCMT) presented by Matthews et al. (2009). Dust grains are expected to have their long axes perpendicular to the magnetic field direction, resulting in polarized thermal emission from anisotropic aligned dust grains (e.g., Lazarian 2007). In Figure 8, we plot the plane-of-sky magnetic field direction in the LBS 23 filament, obtained by rotating the polarization vectors by 90° from the SCUBA JCMT polarization data. The figure shows that the plane-of-sky magnetic field is mostly perpendicular to the filament direction.

We use the dispersion in the distribution of polarization angles to derive the strength of the component of the magnetic field on the plane of the sky ($B_{\rm pos}$) in the LBS 23 region. For

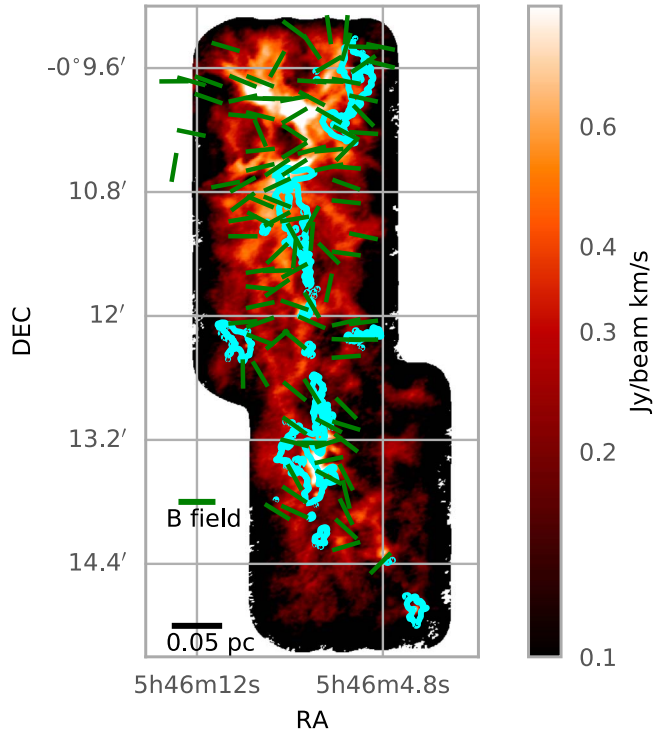

Figure 8. Plane-of-sky magnetic field direction inferred from archival SCUBA JCMT polarization data (Matthews et al. 2009) superposed on an integrated intensity map of the $C^{18}O(2–1)$ emission of the region (color map) and the N_2D^+ peak intensity (contours) from Figure 1(b). Dark green lines represent the direction of the *B*-field derived from the polarization data. All lines are the same length regardless of the polarization percentage.

this, we use the Chandrasekhar–Fermi method (Chandrasekhar & Fermi 1953) and follow Equation (2) in Crutcher et al. (2004):

$$B_{\rm pos} = Q\sqrt{4\pi\rho}\frac{\delta V}{\delta\phi} \approx 9.3\frac{\sqrt{n(H_2)}\,\Delta V}{\delta\phi}\mu G, \quad (5)$$

where $n(H_2)$ is the molecular hydrogen number density of the region, δV is the (average) velocity dispersion of the gas, σ is the dispersion in the polarization position angles, we assume Q to be approximately 0.5 (see below), and $\Delta V = \sqrt{8\ln(2)}\,\delta V$. To estimate the average density of the region, we use our $C^{18}O$ data, as emission from N_2D^+ (a much higher-density tracer) does not cover the entire region where polarization was detected (see Figure 8). We estimate the column density of $C^{18}O$ by following equations in Garden et al. (1991) and Buckle et al. (2010):

$$N_{\rm C^{18}O} = \frac{1.26\times10^{14}}{1-\exp(-10.54/T_{\rm ex})}\frac{T_{\rm ex}+0.88}{J(T_{\rm ex})-J(T_{\rm bg})}\int T_{\rm mb}dv, \quad (6)$$

$$J(T) = \frac{h\nu}{k}\frac{1}{\exp(h\nu/kT)-1}, \quad (7)$$

where T_{mb} is the main beam brightness temperature, T_{ex} is the excitation temperature, and T_{bg} is the background brightness temperature, which is due to cosmic background radiation. We adopt a $C^{18}O$ to H_2 ratio of 1.7×10^{-7} (Hsieh et al. 2019) and assume the depth of the region to be about 0.1 pc (which is about half the width of the JCMT polarization map) in order to estimate an average density of the region of $n(H_2)\sim1.7\times10^4$ cm^{-3}. We made Gaussian fits to the $C^{18}O$ spectra in the region and obtained an average velocity dispersion (δV) of 0.6 km s^{-1}. With a measured polarization angle dispersion ($\delta\phi$) of 36.6°, and using Equation (5), we find the magnetic field strength in the plane of the sky in the medium-density region traced by $C^{18}O$ to be about 50 μG.

Ostriker et al. (2001) conducted MHD simulations and found the value of Q in Equation (5) ranges between 0.46 and 0.51 when the measured dispersion in the polarization angle is less than ∼25°. For such low dispersion, the expected uncertainty in the value of Q is less than 30% (Crutcher et al. 2004). However, it is also important to note that different simulations result in slightly different Q values. For example, the results by Padoan et al. (2001) and Heitsch et al. (2001) give Q ranges between 0.3 and 0.4. Moreover, the Chandrasekhar–Fermi method is not optimal for dense structures where gravitational forces dominate over MHD turbulence. Given these caveats, our method should give us a rough estimate of the magnetic field strength with an uncertainty of factor of a few (e.g., Heitsch 2005). Our estimate is enough to provide a general idea of how the magnetic fields affect the gas dynamics in the region.

Theory predicts that magnetic field strength scales with gas density, such that $B\propto\rho^{\kappa}$, where κ may be as low as 0 and as high as 2/3, depending on the evolutionary stage and geometry of the (collapsing) dense structure (Crutcher 2012). Thus, the magnetic field in the central filament, where the average density is 1.6×10^6 cm^{-3}, is expected to be about 50 to 970 μG (i.e., higher than the magnetic strength in the lower-density region traced by the $C^{18}O$ observations). Here, we will assume that the *B*-field strength in the dense filament is about 510 μG (a value between the two extremes estimated above). This value of the magnetic field strength is similar to that measured in structures in star-forming regions with a density similar to our filament (e.g., Ching et al. 2017; Añez-López et al. 2020; Guerra et al. 2020; Pillai et al. 2020; Wang et al. 2020). Using this value for the *B*-field strength, we then estimate the Alfvén speed ($V_A = B/\sqrt{4\pi\rho}$) to be about 0.54 km s^{-1} in the dense filament. In this region, where the average velocity dispersion (σ_v) is 0.23 km s^{-1}, the magnetic Mach number ($M_{\rm A}=\sigma_v/V_{\rm A}$) is approximately 0.4. This implies that the magnetic field can have a slightly larger impact on the gas dynamics of the filament than the turbulence. We also find that, in this filament, $\beta_{\rm B}=2(M_A/M_s)^2\sim0.4$, where M_s is the sonic Mach number, which has a value of 1.0. This indicates that, as expected, the magnetic pressure in this region is greater than the thermal pressure (e.g., Gammie & Ostriker 1996; Crutcher 1999, 2012; Ching et al. 2017).

Another way to assess the role of magnetic fields in the dynamical evolution of a region is to compare the gravitational energy to the magnetic field energy, given by

$$E_{\rm B} = \frac{1}{2}MV_{\rm A}^2, \quad (8)$$

where $V_{\rm A}$ is the Alfvén speed and M is the mass of the region. For the filament in our study, this results in $E_{\rm B}=3.4\times10^{43}$ erg, using the values derived above. Therefore, the gravitational energy is about two times larger than the magnetic field energy (see Table 1), indicating that the filament is magnetic supercritical (i.e., the magnetic field strength in this

region is not enough to support the filament against gravitational collapse). Even though the magnetic energy is about an order of magnitude larger than the rotational energy of the filament, and as discussed above, the *B*-field in this region is likely to have significant influence on the gas dynamics of this region, magnetic braking should be negligible in LBS 23, as the magnetic field orientation is approximately perpendicular to the rotation axis of the filament.

4.6. Other Interpretations of Velocity Gradients in Filaments, and the Case for Rotation

Different studies have interpreted a velocity gradient perpendicular to a filament's major axis as being caused by different processes, including filament rotation (Olmi & Testi 2002), colliding flows (Henshaw et al. 2013), multiple velocities components along the line of sight (Beuther et al. 2015; Dhabal et al. 2018), and gravitational infall of gas onto filaments with an elliptical cross section (i.e., infall with a preferred direction as opposed to isotropic infall (Dhabal et al. 2018; Chen et al. 2020)). Clearly, care must be taken to reveal the true nature of the velocity gradient across a filament.

Changes in the mean velocity of the gas that appear as velocity gradients along the short axis of filaments in low-mass star-forming regions have been recently reported by various studies (Fernández-López et al. 2014; Dhabal et al. 2018; Chen et al. 2020). An explanation for the existence of the observed velocity structure in several of these filaments is the existence of overlapping multiple velocity components along the line of sight. A good example of this is the filament in the Serpens Main-S region (see Figure 11 of Dhabal et al. 2018), where it can be seen that the emission at different velocities (i.e., different velocity components) lie next to each other, but also cross over at an angle. This is different to the filament in our study, as in the channel maps presented in Figure 4, we do not see any sudden change in direction in the emission structure; the main structure shifts slightly in position in consecutive channels but maintains a north–south direction (see Section 3). It would seem extremely unlikely that many subfilaments with almost the same morphology and the same length would perfectly align next to each other with such a well-ordered velocity structure. We thus can safely rule out that multiple velocity components are the origin of the velocity gradient seen in our filament.

Another explanation discussed in the literature for the observed velocity gradient along the minor axis of a filament is converging flows (e.g., due to compression in a turbulent medium, or compression triggered by external processes such as supernova explosions or stellar winds). In the converging flows scenario, both low-density tracers that probe the environment outside the filament and high-density tracers that probe the filament itself are expected to show similar kinematic structures (e.g., Beuther et al. 2015; Chen et al. 2020). We inspected the intensity weighted velocity (Moment 1) maps of our lower-density gas tracers in our ALMA observations (i.e., $C^{18}O$,^{13}CO, H_2CO, and ^{12}CO), and we do not see any evidence of large-scale flows toward the central filament. There is no clear velocity gradient perpendicular to the major axis of the central filament in these lower-density gas maps.

In addition to this qualitative comparison, we follow the prescription given by Chen et al. (2020) to determine whether the observed velocity gradient is due to turbulent compression. If the dimensionless quantity given by

$$C_v \equiv \frac{\Delta v_h^2}{GM/L} \tag{9}$$

is significantly greater than 1, then the velocity gradient in the filament is likely due to shock compression (Chen et al. 2020). In this equation, Δv_h is half the observed velocity difference across the filament minor axis, and M/L is the filament's linear mass. In our case, we find the velocity difference between the east and west ends of the filament is $\sim$0.6 km s^{-1} (see Figure 5), which gives $\Delta v_h \sim 0.3$ km s^{-1}. We estimate the linear mass of our filament within the region from which we obtain the velocity gradient (see Figure 5(a)) to be 69.5 $M_\odot$/pc, which results in $C_v \approx 0.3$. We, therefore can rule out the scenario where the observed velocity gradient in LBS 23 is due to the convergence of large-scale flows or sheet-like structures created by turbulence compression. Even though, according to Chen et al. (2020), our estimate of C_v should indicate that self-gravity is important in shaping the velocity profile in the filament, we argue below that, although gravity is important in our filament, rotation is a more likely explanation for the observed velocity structure.

A velocity gradient across a filament can also be produced by anisotropic infall in a filament formed inside a flattened structure or slab; see Figure 15 in Dhabal et al. (2018) and Figure 1 in Chen et al. (2020). In order to determine whether the velocity gradient in our filament is due to infall, we consider the expected velocity profile from three different simple (collapse) models that have been used to describe the velocity structure of cores and filaments: (1) a scenario where the observed velocities are dominated by rotational velocities in a dynamically collapsing structure where angular momentum is conserved (e.g., Ohashi et al. 1997); (2) a model of radial freefall collapse (with no rotation) under the influence of a central point mass (e.g., Momose et al. 1998); and (3) a gravitationally contracting filament (as discussed by Chen et al. (2020)). In the first case, where angular momentum ($l = mvr$) is conserved, we expect the velocity profile to be v $\propto r^{-1}$. In the case of freefall collapse under a central point mass, radial velocities are governed by the conservation of energy ($\frac{1}{2}mv^2 = \frac{GMm}{r}$), and we expect $v \propto r^{-0.5}$. The infall velocity for a gravitational contracting filament is given by $v^2 \approx G\,M(r)/L$, where mass is a function of radius ($M(r)$) and length is represented by L; see Equation (3) of Chen et al. (2020). In Figure 7, we fit the density profile and show that $\rho(r) \propto r^{-2}$. In Appendix C, we use the density profile of our filament to derive $M(r) = \pi L \rho_c R_{\rm flat}^2 \left[\ln\left(\frac{R_{\rm flat}^2 + r^2}{R_{\rm flat}^2}\right)\right]$, which would result in an infall velocity profile of $v \propto \sqrt{\ln(1 + (r/R_{\rm flat})^2)}$ for our filament.

We compared the derived specific angular momentum profile of our filament with the specific angular momentum profile one would naively expect to detect if one were to assume that an observed velocity gradient in the three models described above were due to rotation ($j_{\rm obs}(r)$). To do this, we simply multiply the expected velocity profile of the model by r. Thus, for example, $j_{\rm obs}(r)$ for the second model described above would be $vr \propto r^{0.5}$. In Figure 9, we show schematic diagrams of $j_{\rm obs}(r)$ for the first two models listed above and the specific angular momentum profile derived for the central filament in

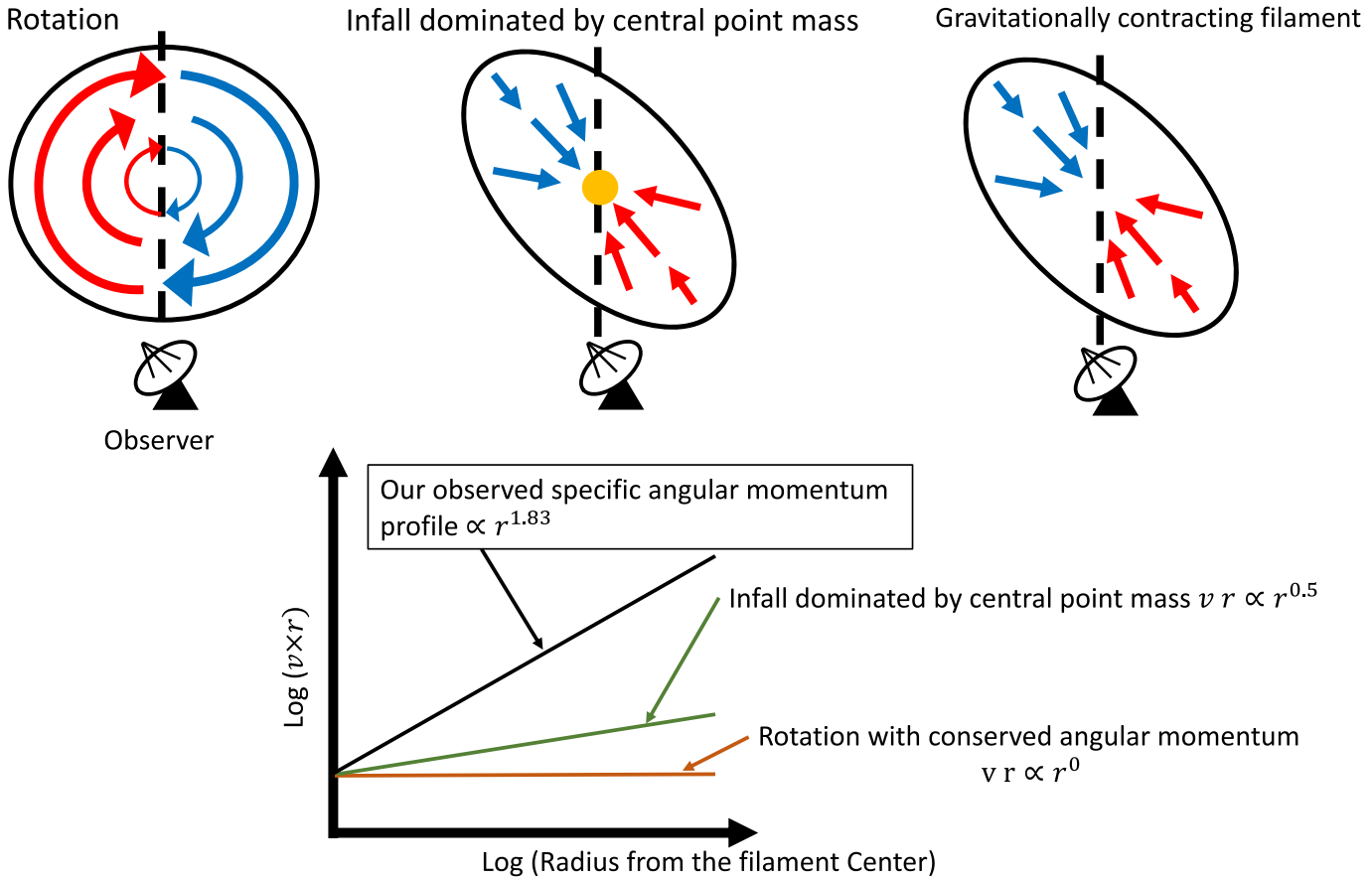

Figure 9. Schematic representation of collapse scenarios discussed in Section 4.6: (1) rotation with conserved angular momentum; (2) infall dominated by point mass; and (3) gravitationally contracting filament. Diagrams are based on Figure 15 of Dhabal et al. (2018). The bottom plot shows a comparison of the expected $r \times v$ profile for the first two models and the profile observed in the filament in this study.

LBS 23. The slope (i.e., the power-law index) of the observed profile in our filament is significantly higher than these two collapse scenarios. In Figure 6, we also compare the derived specific angular momentum profile for our filament and the $j_{\rm obs}(r)$ one would expect for a gravitationally contracting filament with a mass distribution similar to that of the central filament in LBS 23. Again, we see that the derived $j_{\rm obs}(r)$ for our filament is significantly different from that expected from the model. It is therefore unlikely that the detected velocity gradient in the central filament is mainly due to gravitational infall.

Smith et al. (2016) used hydrodynamic turbulent cloud simulations to study the formation and kinematics of filaments in molecular clouds. From these simulations, they were able to decompose the kinematic structure of the filaments into different components, one of which was the rotational velocity. Even though Smith et al. conclude that filaments that form in their simulations do not have ordered rotation on scales of 0.1 pc, they do detect rotational velocities of up to about 0.23 km s^{-1} (similar to the maximum rotational velocity we detect in our filament of 0.3 km s^{-1}), and their filaments show ordered rotation at the scales of a few 0.01 pc similar to the scales of our filament (see Figure 9 in Smith et al. 2016). We are thus confident that rotation in a small filament like the one we studied here is possible.

The velocity structure of the N_2D^+ emission allows us to confidently assert that the observed velocity gradient in the central LBS23 filament is not due to parallel subfilaments at slightly different velocities. Similarly, we are convinced that the filament velocity gradient is not caused by colliding flows, since we do not detect velocity gradients across the filament at larger scales with lower-density gas tracers. Moreover, we discard gravitational collapse as the main cause of the observed velocity gradient, as the derived specific angular momentum profile for our filament significantly deviates from that expected from three different collapse scenarios. We thus conclude that rotation is the most likely scenario, as our filament's $j_{\rm obs}(r)$ is consistent with the specific angular momentum profile observed for cores with velocity gradients that are generally presumed to be due to rotation.

5. Summary and Conclusions

We have analyzed the kinematic structure of a star-forming filament in the HH 24–26 region (a.k.a. LBS23) in Orion B, using ALMA N_2D^+ observations. The data clearly show a gradient along the filament's minor axis, which we argue is caused by rotation in the filament. From this, we obtain a reliable estimate of the specific angular momentum in a rotating star-forming filament, comparable to the specific angular momentum of cores with similar size found in other star-forming regions.

We compared the data with both rotating and nonrotating cylinder models, and found that in both cases, the observed linear mass is higher than the critical linear mass above which the filament (cylinder) is expected to be unstable against collapse. Multiple dust continuum point sources at the ends of

the filament, coincident with high-velocity outflow emission, suggest that there is ongoing star formation taking place in this filament, consistent with the measured high linear mass.

The dependence of the filament specific angular momentum profile as a function of radius ($j(r) \propto r^{1.8}$) is consistent with that observed in cores in other regions of star formation, and it provides evidence that suggests the process that produces the velocity gradients in cores may be similar to what took place in this filament. The power-law dependence of the specific angular momentum with radius in the filament studied here is seen to continue down to scales of several 10^2 au, with no indication of flattening. That is, there is no detectable scale at which the angular momentum is conserved. This suggests that the rotation in this filament may have been set by the turbulence in the cloud at all scales, even down to the scale of the triple system that has formed in this filament. This is consistent with the scenario in which filaments and cores develop simultaneously from the multiscale growth of nonlinear perturbations generated by turbulence, and it is in contrast with the traditional two-step scenario where thermally supercritical filaments form first and then fragment longitudinally into cores.

Filaments, in general, fill the missing scales between cores and cloud. Thus, more measurements of filament angular momentum are needed in order to have a clear picture of how angular momentum is transferred from cloud scales to cores.

We analyzed the turbulence in the central filament and found it to be transonic. This is in contrast with the expected subsonic motions in coherent cores and filaments, where turbulence decays on 0.1 pc scales The existence of a very young protostellar triple system in the filament suggests that star formation can occur even before turbulence decays down to subsonic motions. We further estimated the turbulence energy dissipation rate and found it to be at least an order of magnitude smaller than the typical outflow energy injection rate from protostars in a similar nearby cloud. The excess of outflow energy injection rate may be able to sustain the turbulence in the filament and prevent from further collapse in the future.

Using archival 850 μm JCMT SCUBA polarization data, we find the magnetic field on the plane of the sky in the LBS 23 region is mostly perpendicular to the filament. The orientation of the magnetic field with respect to the filament's rotation axis implies that magnetic breaking effects should be negligible. Using the Chandrasekhar–Fermi method, we estimate the plane-of-sky magnetic field strength in the extended (medium-density) region surrounding the filament to be approximately 50 μG. Following theoretical predictions that indicate magnetic field strength increases with gas density, we speculate that the magnetic field strength in the dense filament should be about a factor of ten larger ($\sim$500 μG), similar to the magnetic field strength determined in other similar high-density regions.

C. H. H. and H. G. A. acknowledge support from the National Science Foundation award AST-1714710. D. M. acknowledges support from CONICYT project Basal AFB170002. The authors thank Simone Recchi and Alvaro Hacar for conducting the calculation and providing the critical linear mass table for additional truncation radii. The authors further thank the NAASC Data Analysts, Sarah Wood and Tom Booth, who helped with data reduction during the face-to-face visit. This paper makes use of the following ALMA data: ADS/JAO.ALMA #2016.1.01338.S ALMA is a partnership of ESO (representing its member states), NSF (USA) and NINS (Japan), together with NRC (Canada), NSC and ASIAA (Taiwan), and KASI (Republic of Korea), in cooperation with the Republic of Chile. The Joint ALMA Observatory is operated by ESO, AUI/NRAO, and NAOJ. The National Radio Astronomy Observatory is a facility of the National Science Foundation operated under cooperative agreement by Associated Universities, Inc.

Software: CASA, astropy.

Appendix A
Column Density Estimation

We use the Herschel-Plank dust optical depth map from Lombardi et al. (2014) and our N_2D^+ ALMA map to estimate the H_2 column density of the filament, based on the method used by Hacar et al. (2018) using N_2H^+ data and Herschel-Plank dust continuum emission maps in Orion A. The 850 μm optical depth map, which has an angular resolution of 36.″0 over the region of interest, was first converted to *K*-band extinction (A_K) using the expression:

$$A_K = \gamma \tau_{850} + \delta, \tag{A1}$$

where $\gamma_{\mathrm{Orion}B} = 3460$ mag and $\delta_{\mathrm{Orion}B} = -0.001$ mag (see Equation (11) in Lombardi et al. 2014). Following Hacar et al. (2017), we then find the column density by converting the *K*-band extinction to *V*-band extinction, using $A_V/A_K = 8.933$ (Rieke & Lebofsky 1985), and converting A_V into H_2 column density, using $N(H_2)/A_V = 0.93 \times 10^{21}$ cm^{-2} mag^{-1} (Bohlin et al. 1978).

We then compare our N_2D^+ data with the derived column density map in order to estimate the mass of the filaments. To do this, we first produced an integrated intensity map of the ALMA N_2D^+ Total Power data by integrating over velocities where there is significant emission (i.e., from $V_{lsr} = 8.4$ km s^{-1} to about 11.3 km s^{-1}). We then smoothed the N_2D^+ integrated intensity map, which has a resolution of 28.″2, to match the resolution of the derived column density map, using the CASA command *imsmooth*. We regridded both maps so that they have the same (equatorial) coordinate and (Nyquist-sampled) pixel scale, and obtained the values of the column density and the N_2D^+ integrated intensity ($W(N_2D^+)$) for each position (i.e., pixel). In Figure 10, we show a scatter plot of these values, where a clear correlation between the H_2 column density and N_2D^+ integrated intensity is detected. A line fit to the data:

$$N(\mathrm{H_2}) = m \times W((\mathrm{N_2D^+}) + C \tag{A2}$$

gives the best-fit parameters as $m = (8.97 \pm 0.56) \times 10^{24}$ cm^{-2}(Jy arcsec^{-2} km s^{-1})$^{-1}$ and $C = (1.62 \pm 0.15) \times 10^{22}$ cm^{-2}. We then applied this empirical relationship to the high-resolution N_2D^+ integrated intensity (Moment 0) map (Figure 1(a)). The final (high-resolution) column density map is shown in Figure 1(a). The mass can then be obtained using this map and the following formula:

$$M(\mathrm{H_2}) = 2\mu m_p N(\mathrm{H_2}) A, \tag{A3}$$

where $\mu = 1.37$, $m_p = 1.67 \times 10^{-24}$ g is the proton mass, and A is the area of interest.

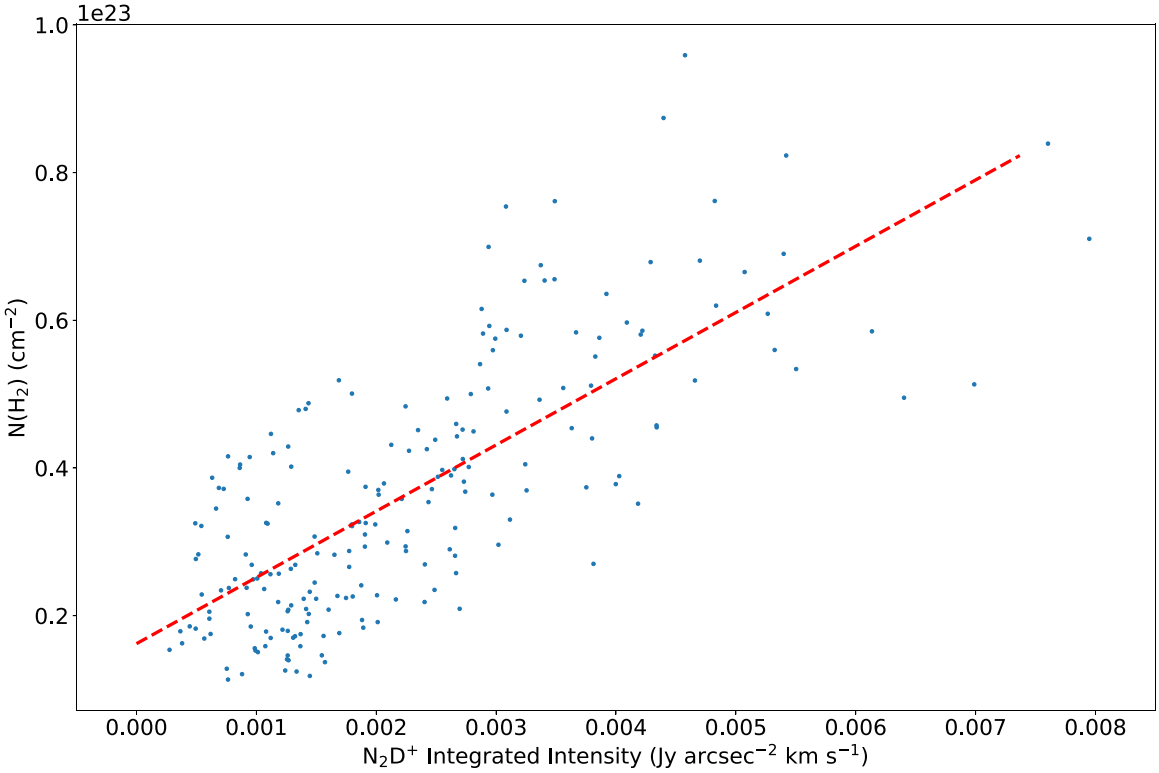

Figure 10. Empirical relation between the H_2 column density map obtained from the Herschel–Planck dust continuum map and the N_2D^+ integrated intensity from the ALMA total power observations. Each point represents the value of $N(H_2)$ and $W(N_2D^+)$ at the same position in the maps. Red dashed line shows the line fit to the points.

Appendix B
Abundance Ratio Estimation

We follow the formalism in Caselli et al. (2002) to estimate the N_2D^+ column density from the line emission. For an optically thin line, the column density can be expressed as:

$$N_{N_2D^+} = \frac{C}{J_\nu(T_{ex}) - J_\nu(T_{bg})} \frac{1}{1 - e^{h\nu/kT_{ex}}} \frac{Q_{\rm rot}}{g_l e^{-E_l/kT_{ex}}}, \quad \text{(B1)}$$

where

$$C = \frac{8\pi W}{\lambda^3 A_{ul}} \times \frac{g_l}{g_u} \quad \text{(B2)}$$

$$J(T) = \frac{h\nu}{k} \frac{1}{\exp(h\nu/kT) - 1} \quad \text{(B3)}$$

$$Q_{\rm rot} = \sum_{J=0}^{\infty} (2J + 1)\exp(-E_J/kT) \quad \text{(B4)}$$

$$E_J = J(J + 1)hB. \quad \text{(B5)}$$

In the equations above, $Q_{\rm rot}$ is the partition function,[10] W is the integrated intensity of the line (in $\rm K\,km\,s^{-1}$), $B = 38554.719$ MHz is the rotational constant (Caselli et al. 2002), and $A_{ul} = 7.138 \times 10^{-4}\,\rm s^{-1}$ is the Einstein coefficient for the $J = 3 - 2$ transition (Pagani et al. 2009; Redaelli et al. 2019). In the calculation, we assume the excitation temperature to be 10 K. After obtaining the column density map of N_2D^+, we divide the total column density estimated from the Herschel-Plank map (see Appendix A above) to find the N_2D^+/H_2 abundance ratio, which we show in Figure 11(b). The N_2D^+/H_2 abundance ratio ranges between (6–8) $\times 10^{-12}$, which is similar to the N_2D^+ abundance observed in other cold dense regions (e.g., Tatematsu et al. 2020).

[10] Note that the partition function of rotational transitions neglecting the hyperfine structure is different from the hyperfine partition function (see Appendix A in Redaelli et al. 2019). We use the former, as we do not resolve the individual hyperfine lines in our observations of the N_2D^+ $J = 3 - 2$ rotational transition.

Appendix C
Gravitational and Rotational Energy Estimation

Here, we describe our procedure for estimating the rotational and gravitational energies of the filament. Consider a rotating cylindrical filament with mass M, radius R, and length L. The rotational axis is along the direction of the cylinder's length. The rotational energy is given by:

$$E_{\rm rot} = \frac{1}{2} I\omega^2. \quad \text{(C1)}$$

In our case, we need to obtain the moment of inertia (I) for a cylinder with a nonuniform density. The equation for the surface density of an idealized cylindrical filament with a Plummer-like profile is:

$$\Sigma(r) = \frac{A_p \rho_c R_{\rm flat}}{\left[\left(1 + \left(\frac{r}{R_{\rm flat}}\right)^2\right)\right]^{(p-1)/2}}, \quad \text{(C2)}$$

and the corresponding radial density profile is given by:

$$\rho_{\rm p}(r) = \frac{\rho_{\rm c}}{[1 + (r/R_{\rm flat})^2]^{p/2}}, \quad \text{(C3)}$$

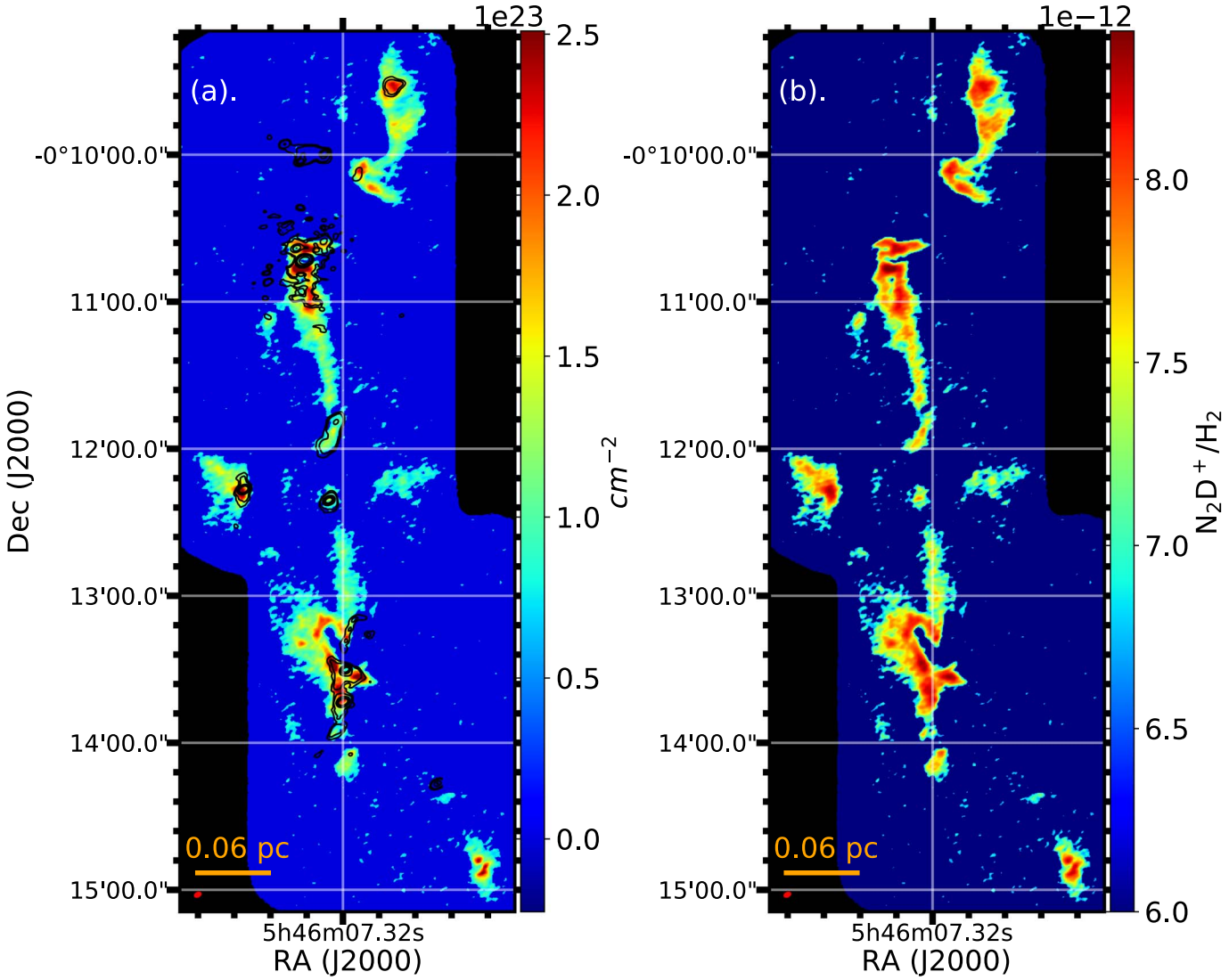

Figure 11. (a). High-resolution H_2 column density map obtained using the ALMA high-resolution N_2D^+ integrated intensity map (Figure 1(a)) and the empirical relation derived in Figure 10. Black contours show the 1.29 mm dust continuum emission in steps of 3σ, 5σ, 20σ, 40σ, 80σ, 320σ, where $\sigma = 5.4 \times 10^{-4}$ Jy beam^{-1} (b). Map of the N_2D^+/H_2 abundance ratio. The size of the synthesized beam is represented with a red ellipse in the lower left corner of each panel.

where

$$A_{\rm p} = \frac{1}{\cos i} \int_{-\infty}^{\infty} \frac{{\rm d}u}{(1+u^2)^{p/2}}$$

(Arzoumanian et al. 2011). We consider our filament to be on the plane of sky ($i = 0°$). In Section 4.3, we fit the column density of the central filament with a Plummer-like profile given by Equation (3) (see Figure 7). Using $p = 2$ (see Section 4.4), we find $A_p = \pi$. Using our estimate of N_0 and $R_{\rm flat} = 0.006$ pc (both obtained from our fit to Equation (3)), and using $\Sigma = \mu m_H N_{H_2}$, where m_H is the hydrogen mass and $\mu = 2.33$ is the mean molecular mass (Arzoumanian et al. 2011), we then obtain an estimate for the central density, ρ_c (in Equation (C3)), of 9.88×10^{-18} g cm^{-3}.

We then use the density profile to obtain the momentum of inertia (I):

$$I = \int_0^R r^2 \rho(r) dV = \int_0^R r^2 2\pi r \rho(r) L dr \tag{C4}$$

$$= 2\pi L \int_0^R r^3 \times \frac{\rho_c}{1 + (r/R_{\rm flat})^2} dr \tag{C5}$$

$$= \pi L \rho_c R_{\rm flat}^2 \left[R^2 - R_{\rm flat}^2 \ln\left(\frac{R_{\rm flat}^2 + R^2}{R_{\rm flat}^2} \right) \right]. \tag{C6}$$

The mass of a cylindrical filament with a density profile given by Equation (C3) can be obtained with the following equation:

$$M = \int_0^R 2\pi r \rho(r) L dr \tag{C7}$$

$$= 2\pi L \int_0^R r \times \frac{\rho_c}{1 + (r/R_{\rm flat})^2} dr \quad \text{(C8)}$$

$$= \pi L \rho_c R_{\rm flat}^2 \left[\ln\left(\frac{R_{\rm flat}^2 + R^2}{R_{\rm flat}^2} \right) \right]. \quad \text{(C9)}$$

Using Equation (C9) in Equation (C6), we can get an expression for I in terms of the filament mass M (and independent of L):

$$I = \frac{M}{\ln\left(\frac{R_{\rm flat}^2 + R^2}{R_{\rm flat}^2} \right)} \left[R^2 - R_{\rm flat}^2 \ln\left(\frac{R_{\rm flat}^2 + R^2}{R_{\rm flat}^2} \right) \right]. \quad \text{(C10)}$$

For our filament $M = 11.7\ M_\odot$, $R_{\rm flat} = 0.06$ pc, the average radius is $R = 2770$ au and $\omega = 6.5 \times 10^{-13}$ rad s^{-1}. Hence, the rotational energy of the filament is 3.0×10^{42} erg.

The gravitational energy in a filament is given by:

$$E_G = -\frac{GM^2}{L}, \quad \text{(C11)}$$

where, again, M and L are the mass and length of the filament (Fiege & Pudritz 2000). For our filament, $L \sim 34,000$ au, which results in an estimate of the gravitational energy of -7.1×10^{43} erg. Therefore, the ratio of the rotational energy to gravitational energy ($\beta_{\rm rot}$) is ~0.04.

ORCID iDs

Cheng-Han Hsieh (承翰) https://orcid.org/0000-0003-2803-6358
Héctor G. Arce https://orcid.org/0000-0001-5653-7817
Diego Mardones https://orcid.org/0000-0002-5065-9175
Shuo Kong https://orcid.org/0000-0002-8469-2029
Adele Plunkett https://orcid.org/0000-0002-9912-5705

References

André, P., di Francesco, J., Ward-Thompson, D., et al. 2014, in Protostars and Planets VI, ed. H. Beuther et al. (Tucson, AZ: Univ. Arizona Press), 27
André, P., Könyves, V., Arzoumanian, D., et al. 2013, ASP Conf. Ser. 476, New Trends in Radio Astronomy in the ALMA Era: The 30th Anniversary of Nobeyama Radio Observatory (San Francisco, CA: ASP), 95
André, P., Men'shchikov, A., Bontemps, S., et al. 2010, A&A, 518, L102
Añez-López, N., Busquet, G., Koch, P. M., et al. 2020, A&A, 644, A52
Arce, H. G., Borkin, M. A., Goodman, A. A., et al. 2011, ApJ, 742, 105
Arzoumanian, D., André, P., Didelon, P., et al. 2011, A&A, 529, L6
Arzoumanian, D., André, P., Könyves, V., et al. 2019, A&A, 621, A42
Barranco, J. A., & Goodman, A. A. 1998, ApJ, 504, 207
Basu, S. 1997, ApJ, 485, 240
Basu, S., & Mouschovias, T. C. 1994, ApJ, 432, 720
Bate, M. R. 2011, MNRAS, 417, 2036
Bate, M. R. 2018, MNRAS, 475, 5618
Belloche, A. 2013, in EAS Publications Series 62, Role and Mechanisms of Angular Momentum Transport During the Formation and Early Evolution of Stars, ed. P. Hennebelle & C. Charbonnel (Cambridge: Cambridge Univ. Press), 25
Belloche, A., André, P., Despois, D., et al. 2002, A&A, 393, 927
Beuther, H., Ragan, S. E., Johnston, K., et al. 2015, A&A, 584, A67
Bohlin, R. C., Savage, B. D., & Drake, J. F. 1978, ApJ, 224, 132
Boss, A. P. 1999, ApJ, 520, 744
Buckle, J. V., Curtis, E. I., Roberts, J. F., et al. 2010, MNRAS, 401, 204
Burkert, A., & Bodenheimer, P. 2000, ApJ, 543, 822
Caselli, P., Benson, P. J., Myers, P. C., et al. 2002, ApJ, 572, 238
Caselli, P., Walmsley, C. M., Zucconi, A., et al. 2002, ApJ, 565, 344
Chandrasekhar, S., & Fermi, E. 1953, ApJ, 118, 113
Chen, C.-Y., Mundy, L. G., Ostriker, E. C., et al. 2020, MNRAS, 494, 3675
Chen, C.-Y., & Ostriker, E. C. 2014, ApJ, 785, 69
Chen, C.-Y., & Ostriker, E. C. 2015, ApJ, 810, 126
Chen, C.-Y., & Ostriker, E. C. 2018, ApJ, 865, 34
Chen, X., Arce, H. G., Zhang, Q., et al. 2013, ApJ, 768, 110
Chen, X., Launhardt, R., & Henning, T. 2007, ApJ, 669, 1058
Ching, T.-C., Lai, S.-P., Zhang, Q., et al. 2017, ApJ, 838, 121
Chini, R., Krugel, E., Haslam, C. G. T., et al. 1993, A&A, 272, L5
Crutcher, R. M. 1999, ApJ, 520, 706
Crutcher, R. M. 2012, ARA&A, 50, 29
Crutcher, R. M., Nutter, D. J., Ward-Thompson, D., et al. 2004, ApJ, 600, 279
Dhabal, A., Mundy, L. G., Rizzo, M. J., et al. 2018, ApJ, 853, 169
Dib, S., Hennebelle, P., Pineda, J. E., et al. 2010, ApJ, 723, 425
Feddersen, J. R., Arce, H. G., Kong, S., et al. 2020, ApJ, 896, 11
Federrath, C. 2016, MNRAS, 457, 375
Fernández-López, M., Arce, H. G., Looney, L., et al. 2014, ApJL, 790, L19
Fiege, J. D., & Pudritz, R. E. 2000, MNRAS, 311, 85
Friesen, R. K., Bourke, T. L., Di Francesco, J., et al. 2016, ApJ, 833, 204
Friesen, R. K., Di Francesco, J., Myers, P. C., et al. 2010, ApJ, 718, 666
Furlan, E., Fischer, W. J., Ali, B., et al. 2016, ApJS, 224, 5
Gammie, C. F., & Ostriker, E. C. 1996, ApJ, 466, 814
Garden, R. P., Hayashi, M., Gatley, I., et al. 1991, ApJ, 374, 540
Gaudel, M., Maury, A. J., Belloche, A., et al. 2020, A&A, 637, A92
Gerin, M., Pearson, J. C., Roueff, E., et al. 2001, ApJL, 551, L193
Gómez, G. C., & Vázquez-Semadeni, E. 2014, ApJ, 791, 124
Gong, H., & Ostriker, E. C. 2011, ApJ, 729, 120
Gong, M., & Ostriker, E. C. 2015, ApJ, 806, 31
Goodman, A. A., Barranco, J. A., Wilner, D. J., et al. 1998, ApJ, 504, 223
Goodman, A. A., Benson, P. J., Fuller, G. A., et al. 1993, ApJ, 406, 528
Guerra, J. A., Chuss, D. T., Dowell, C. D., et al. 2020, arXiv:2007.04923
Hacar, A., Tafalla, M., & Alves, J. 2017, A&A, 606, A123
Hacar, A., Tafalla, M., Forbrich, J., et al. 2018, A&A, 610, A77
Heitsch, F. 2005, in ASP Conf. Ser. 343, Astronomical Polarimetry: Current Status and Future Directions, ed. A. Adamson et al. (San Francisco, CA: ASP), 166
Heitsch, F., Zweibel, E. G., Mac Low, M.-M., et al. 2001, ApJ, 561, 800
Henshaw, J. D., Caselli, P., Fontani, F., et al. 2013, MNRAS, 428, 3425
Hsieh, C.-. han., Hu, Y., Lai, S.-P., et al. 2019, ApJ, 873, 16
Inagaki, S., & Hachisu, I. 1978, PASJ, 30, 39
Inutsuka, S.-I., & Miyama, S. M. 1992, ApJ, 388, 392
Inutsuka, S.-. ichiro., & Miyama, S. M. 1997, ApJ, 480, 681
Jappsen, A.-K., & Klessen, R. S. 2004, A&A, 423, 1
Jijina, J., Myers, P. C., & Adams, F. C. 1999, ApJS, 125, 161
Kainulainen, J., Hacar, A., Alves, J., et al. 2016, A&A, 586, A27
Koch, E. W., & Rosolowsky, E. W. 2015, MNRAS, 452, 3435
Kong, S., Caselli, P., Tan, J. C., et al. 2015, ApJ, 804, 98
Kong, S., Tan, J. C., Caselli, P., et al. 2017, ApJ, 834, 193
Kong, S., Tan, J. C., Caselli, P., et al. 2018, ApJ, 867, 94
Kurono, Y., Saito, M., Kamazaki, T., et al. 2013, ApJ, 765, 85
Kuznetsova, A., Hartmann, L., & Heitsch, F. 2019, ApJ, 876, 33
Lada, E. A., Bally, J., & Stark, A. A. 1991, ApJ, 368, 432
Larson, R. B. 2003, RPPh, 66, 1651
Lazarian, A. 2007, JQSRT, 106, 225
Levshakov, S. A., Reimers, D., & Henkel, C. 2016, A&A, 586, A126
Li, Z.-Y., Banerjee, R., Pudritz, R. E., et al. 2014, in Protostars and Planets VI, ed. H. Beuther et al. (Tucson, AZ: Univ. Arizona Press), 173
Li, Z.-Y., Krasnopolsky, R., & Shang, H. 2011, ApJ, 738, 180
Linsky, J. L., Draine, B. T., Moos, H. W., et al. 2006, ApJ, 647, 1106
Lique, F., Daniel, F., Pagani, L., et al. 2015, MNRAS, 446, 1245
Lis, D. C., Menten, K. M., & Zylka, R. 1999, ApJ, 527, 856
Lombardi, M., Bouy, H., Alves, J., et al. 2014, A&A, 566, A45
Mac Low, M.-M. 1999, ApJ, 524, 169
Matthews, B. C., McPhee, C. A., Fissel, L. M., et al. 2009, ApJS, 182, 143
McKee, C. F. 1989, ApJ, 345, 782
Megeath, S. T., Gutermuth, R., Muzerolle, J., et al. 2012, AJ, 144, 192
Meng, F., Wu, Y., & Liu, T. 2013, ApJS, 209, 37
Misugi, Y., Inutsuka, S.-. ichiro., & Arzoumanian, D. 2019, ApJ, 881, 11
Momose, M., Ohashi, N., Kawabe, R., et al. 1998, ApJ, 504, 314
Myers, P. C., Evans, N. J., & Ohashi, N. 2000, in Protostars and Planets IV, ed. V. Mannings, A. P. Boss, & S. S. Russell (Tucson, AZ: Univ. Arizona Press), 217
Offner, S. S. R., Klein, R. I., & McKee, C. F. 2008, ApJ, 686, 1174
Ohashi, N., Hayashi, M., Ho, P. T. P., et al. 1997, ApJ, 488, 317
Olmi, L., & Testi, L. 2002, A&A, 392, 1053
Ostriker, E. C., Stone, J. M., & Gammie, C. F. 2001, ApJ, 546, 980
Ostriker, J. 1964, ApJ, 140, 1056
Padoan, P., Goodman, A., Draine, B. T., et al. 2001, ApJ, 559, 1005
Pagani, L., Bacmann, A., Cabrit, S., et al. 2007, A&A, 467, 179
Pagani, L., Daniel, F., & Dubernet, M.-L. 2009, A&A, 494, 719

Palmeirim, P., André, P., Kirk, J., et al. 2013, A&A, 550, A38
Pillai, T. G. S., Clemens, D. P., Reissl, S., et al. 2020, NatAs, 4, 1195
Pineda, J. E., Goodman, A. A., Arce, H. G., et al. 2010, ApJL, 712, L116
Pineda, J. E., Zhao, B., Schmiedeke, A., et al. 2019, ApJ, 882, 103
Pon, A., Toalá, J. A., Johnstone, D., et al. 2012, ApJ, 756, 145
Recchi, S., Hacar, A., & Palestini, A. 2014, MNRAS, 444, 1775
Redaelli, E., Bizzocchi, L., Caselli, P., et al. 2019, A&A, 629, A15
Rieke, G. H., & Lebofsky, M. J. 1985, ApJ, 288, 618
Smith, R. J., Glover, S. C. O., & Klessen, R. S. 2014, MNRAS, 445, 2900
Smith, R. J., Glover, S. C. O., Klessen, R. S., et al. 2016, MNRAS, 455, 3640
Suri, S., Sánchez-Monge, Á, Schilke, P., et al. 2019, A&A, 623, A142
Tafalla, M., & Hacar, A. 2015, A&A, 574, A104
Tatematsu, K., Liu, T., Kim, G., et al. 2020, ApJ, 895, 119
Tatematsu, K., Ohashi, S., Sanhueza, P., et al. 2016, PASJ, 68, 24
Tielens, A. G. G. M. 2005, The Physics and Chemistry of the Interstellar Medium (Cambridge: Cambridge Univ. Press)
Tobin, J. J., Bergin, E. A., Hartmann, L., et al. 2013, ApJ, 765, 18
Tobin, J. J., Hartmann, L., Bergin, E., et al. 2012, ApJ, 748, 16
Tobin, J. J., Looney, L. W., Li, Z.-Y., et al. 2016, ApJ, 818, 73
Van Loo, S., Keto, E., & Zhang, Q. 2014, ApJ, 789, 37
Wang, J.-W., Koch, P. M., Galván-Madrid, R., et al. 2020, ApJ, 905, 158
Ward-Thompson, D., Chini, R., Krugel, E., et al. 1995, MNRAS, 274, 1219
Yen, H.-W., Takakuwa, S., Koch, P. M., et al. 2015, ApJ, 812, 129
Zhang, S., Hartmann, L., Zamora-Avilés, M., et al. 2018, MNRAS, 480, 5495